We are IntechOpen,
the world's leading publisher of
Open Access books
Built by scientists, for scientists

5,300
Open access books available

130,000
International authors and editors

155M
Downloads

Our authors are among the

154
Countries delivered to

TOP 1%
most cited scientists

12.2%
Contributors from top 500 universities

CLARIVATE ANALYTICS
BOOK CITATION INDEX
INDEXED

WEB OF SCIENCE™

Selection of our books indexed in the Book Citation Index
in Web of Science™ Core Collection (BKCI)

Interested in publishing with us?
Contact book.department@intechopen.com

High Resolution ^{3}He Pulmonary MRI

Matthew S. Fox and Alexei V. Ouriadov

Abstract

Hyperpolarized gas MRI of the mouse lung is of great interest due to the urgent need for novel biomarkers for the assessment of respiratory-disease progression and development of new therapies. Small animal ^{3}He lung MRI requires high-spatial-resolution imaging (<500 μm) to obtain acceptable images for visualization of all branches of lung microstructure from the mouse trachea to lung parenchyma. The use of conventional fast-gradient-recalled echo (FGRE) pulse sequences for high-spatial-resolution mouse lung imaging is challenging due to the signal loss caused by significant diffusion-weighting by the imaging gradients, particularly in larger airways where ^{3}He diffusion is maximized. In this chapter, a modified FGRE approach called X-Centric is described for acquiring ^{3}He mouse lung MRI. X-Centric is a center-out technique, allowing high-spatial-resolution, and high signal-to-noise ratio density-weighted imaging, as it is a short-TE method minimizing diffusion decay. Here, we also take advantage of a high-performance insertable-gradient-set interfaced with a clinical MRI system and a custom-built constant-volume ventilator to get the maximum benefits of X-Centric. High-spatial-resolution ^{3}He X-Centric imaging was performed in a phantom and mouse lungs, yielding a nominal resolution of 39 μm and 78 μm respectively. We also demonstrate the feasibility of ^{129}Xe/^{19}F X-Centric MRI in a phantom and in rat lungs.

Keywords: X-Centric, ^{3}He, ^{129}X, ^{19}F mouse, rat, lung, short-TE, x-nuclei, pre-clinical, hyperpolarized, MRI, COPD, CF, BPD, alpha-1 antitrypsin deficiency

1. Introduction

Inhaled hyperpolarized gas lung MRI [1] was proven to be useful for the observation and treatment planning of several pulmonary diseases including chronic obstructive pulmonary disease (COPD) [2–6], asthma, [7–11] and lung cancer [12]. With the combined economic burden of COPD and asthma in Canada, Ontario being $5.7 billion (2011) [13], and lung cancer being the leading cause of cancer deaths worldwide, [14] there has been a growing interest in developing new lung imaging techniques such as hyperpolarized ^{3}He and ^{129}Xe MRI as well as hyperpolarized propane (^{1}H) MRI [15, 16] and thermally polarized inert fluorinated gas (^{19}F) MRI [17–19] to better understand various lung diseases.

Our main focus will be on ^{3}He gas MRI of small animal models of lung disease [20, 21], as it is a promising tool to quantify airway and ventilation abnormalities associated with bronchoconstriction, airway narrowing, and subsequent bronchodilation [22, 23]. Small animal ^{3}He lung MRI normally assumes high spatial

resolution imaging (<500 μm [22]) in order to obtain acceptable images for the quantitative analysis and visualization of rodent airways and lung parenchyma. However, high-resolution hyperpolarized gas MR imaging has a number of signal-to-noise ratio (SNR) limitations due to the non-renewable nature of the non-equilibrium magnetization, requiring a minimized number of small flip angle radio-frequency (RF) pulses and quite short image acquisition times during a breath-hold which should be as short as a second in duration for the case of mouse lung imaging. Coupled with the issues of high-resolution imaging are the effects of fast diffusion of ^{3}He (~2 cm^2/s) through strong spatial encoding gradients, which can completely destroy the MRI signal in the airways and significantly attenuate the signal in the lung parenchyma [24–26]. There is a need for an imaging method which incorporates specific hardware and novel rapid image acquisition approaches that minimize the signal loss due to all of these mitigating factors and permit fast and high spatial resolution ^{3}He MR imaging of small animal airways and lung microstructure [27]. Such imaging modalities can be used for observation of ventilation heterogeneity, such as in an ovalbumin asthmatic mouse model [22, 27], as well as for pediatric lung applications [28] often requiring much smaller field-of-view (FOV).

The projection-reconstruction (PR) approach is the well-known [29] acquisition method that minimizes ^{3}He diffusion-induced signal decay, as it acquires the k-space center immediately following the excitation pulse and before the imaging gradient starts which avoids significant signal loss occurs [27]. Both PR and spiral/cones acquisitions belong to free induction decay based or apparent transverse relaxation time (T_2^*) based methods, acquiring k-space in a non-Cartesian fashion. It has been demonstrated that those methods reduce diffusion-weighting for ^{3}He MRI of rodent lungs [22, 30–34]. In addition, they ensure very short echo-times ((TE) < 200 μs) which minimizes T_2^*-weighting, leading to pure gas density weighting [35]. Unfortunately, PR uses a significant number of RF pulses (50,640 views for a 128 × 128 × 128 matrix size and 204,196 for a 256 × 256 × 256 matrix size [36]) or radial projections to sufficiently sample k-space and this naturally leads to reduction of the available SNR from the non-renewable hyperpolarized state [27]. Cones [34] and spiral [28] k-space trajectories normally do not require a significant number of RF tipping or interleaves to fill k-space, but this should still be compensated by using an elongated readout-window which can be difficult to achieve due to the short T_2^* of ^{3}He gas in small animal lungs (T_2^* < 3 ms, at high field [37]). Commonly, non-Cartesian acquisitions require dedicated k-space interpolating and regridding as well as density-weighting procedures for image reconstruction [27], which often can have smoothing effects and resolution implications. Furthermore, non-Cartesian traversal of k-space by either PR or spiral/cones often requires significant oversampling, which leads to commensurate increases in acquisition time and consequently prohibiting single breath-hold imaging in rodents. Driehuys et al. [22] suggests that ^{3}He MRI measurements of rapid dynamic changes in mouse lungs followed by methacholine challenge can be done more time and cost efficiently with fast 2D Cartesian imaging compared to 3D PR.

An alternative to PR (which may suffer from poor edge resolution and sampling/reconstruction artifacts [18]) for high spatial resolution single-breath 2D imaging of small animal lung employs two separate excitations with inverted read-out gradients to acquire both halves of Cartesian k-space in a center-out fashion to minimize both diffusion-weighting [38, 39] and T_2^*-weighting [17]. This technique is known as the X-Centric method [27, 39]. It uses a well-known Fast Gradient-Recalled Echo (FGRE) sequence as its basis [27, 39], so the method can be relatively easy implemented on any clinical MRI scanners [17, 27]. Also, because X-Centric is a Cartesian method, it does not require interpolating, regridding and density-weighting procedures for image reconstruction [17, 27, 39]. It minimizes both

gradient-induced diffusion attenuation [27, 39] and T_2^*-based signal attenuation [17] at the center of k-space, and does not depend on the image resolution for a chosen FOV and bandwidth (BW_{read}).

In this chapter we present an X-Centric approach developed for a single breath-hold high spatial resolution ^{3}He MRI of mouse lungs. The method takes advantage of a high performance insertable gradient set interfaced with a clinical MRI system and precise custom built constant-volume ventilator. The X-Centric approach is compared to partial-echo FGRE [25] on the basis of SNR efficiency over a range of spatial resolutions in a phantom [27]. The robustness of the X-Centric technique for ^{3}He in-vivo lung imaging of mice is demonstrated [27]. The feasibility of the X-Centric approach to image dissolved hyperpolarized ^{129}Xe in a phantom and with ^{19}F gas in a rat lung [17] is also demonstrated in this chapter.

2. Theoretical background

2.1 ^{3}He MRI

Table 1 summarizes the physical properties of the ^{3}He isotope along with other gases used for inhaled lung MRI [40] such as ^{129}Xe [1, 41], inert fluorinated gases possessing ^{19}F spins [17–19] and propane [16] which is proton-based (^{1}H). It is well-known, that helium gas has the highest self-diffusion coefficient (D), which is around 2 cm^2/s for pure helium, and it is around 0.9 cm^2/s, when helium diffuses in air or is part of a helium/air mixture. Its very high diffusivity suggests that high-resolution ^{3}He MRI can be quite challenging due to the induced decay of the MR signal by the applied imaging gradients [22, 24]. However, signal attenuation due to diffusion is not the only reason making high-resolution ^{3}He MRI problematic. In most cases it requires very careful consideration of all MRI related physical properties of ^{3}He and sequence parameter effects, such as the contribution of relaxation times to both signal decay and image blurring [42]. In addition to these

Parameter	C_3H_8 (^{1}H)	SF_6 (^{19}F)	^{3}He	^{129}Xe
Nuclear spin, I	1/2	1/2	1/2	1/2
Gyromagnetic ratio, (MHz rad/T)	267.5	251.6	203.7	74.5
Natural abundance (%)	100	95	1.4×10^{-4}	26
Apparent transverse relaxation time, T_2^* (ms)	>1.0	0.5[a]/2.0[b]	1.5[a]/3.2[b]	2.8[a]/2.9[c]
Longitudinal relaxation time, T_1 (s)	5.0	30	90[d]	25[d]
Self-diffusion coef., D_0 (cm^2/s)	10^{-3}	0.033	2.05	0.061
Diffusion coef. in air, D (cm^2/s)	0.098	0.094	0.86	0.14
b-Values, (s/cm^2)	12	12	1.6	9
Chemical shift range, $\Delta\delta$ (ppm)	20	150	0.8	220
Ostwald solubility $\times 10^{-4}$, L	61	54	850	1700
Cost, per liter	$20	$20	$800	$20/200[e]

SF_6 and ^{3}He T_2^* values shown within major airway[a] and parenchema[b] of the rodent lung. ^{129}Xe T_2^* values shown for xenon gas[a] within the major airway and xenon dissolved[c] within lung tissue (barrier) and red blood cells. ^{129}Xe and ^{3}He T_1 values[d] measured in rodent lungs after several wash-out (anoxic) breaths of the hyperpolarized gas. Cost of the 86% enriched ^{129}Xe[e].

Table 1.
Comparison of ^{3}He, ^{129}Xe, inert fluorinated gas and propane.

considerations, one needs to consider the use of special MRI hardware such as a high-performance high-slew-rate imaging gradient set [43] and a very high precision ventilator [27] for in-vivo high-resolution imaging. The high diffusivity of ^{3}He as well as its short relaxation times and MRI hardware limitations should all be taken into account for the proper choice of the pulse sequence when high spatial resolution ^{3}He MRI is the goal.

2.2 Relaxation times

Generally, both longitudinal and apparent transverse relaxation [44] times (T_1 and T_2^*) of ^{3}He are not physical constants and they both depend on the main magnetic field strength, its gradients, presence of paramagnetic impurities interacting with the hyperpolarized gas (e.g., oxygen), and finally, diffusivity. Normally, the main mechanism for T_1 decay of hyperpolarized gases (i.e., polarization losses in contrast to conventional thermally polarized spins) is the presence of oxygen in lung [45]. The T_1 decay rate is inversely proportional to the partial oxygen pressure (pO$_2$) [46]:

$$\frac{1}{T_1} = \frac{1}{T_{1,0}} + \kappa \int\limits_0^{time} pO_2(t)dt \tag{1}$$

where $T_{1,0}$ is the longitudinal relaxation time expected in the absence of O$_2$ and κ is the relaxivity of ^{3}He due to the presence of O$_2$ (0.38 atm^{-1} s^{-1} at body temperature [46]).

This suggests that a small number of anoxic pre-breaths or wash-out breaths prior the actual ^{3}He MRI measurements can be helpful for minimizing the oxygen concentration in lung prior to acquisition and administration of hyperpolarized gas. **Table 1** suggests that the T_1 in small animal lungs after applying a number of wash-out breaths can be sufficiently long [47] compared to the typical image acquisition times of 1 s [27] for mice and 10 s for rats [37]. As previous work shows, eight wash-out breaths drastically reduce the O$_2$ concentration [17, 23, 48]. The value of T_2^* for ^{3}He normally varies between the major airways (1.5 ± 0.25 ms [37]) and lung parenchyma (3.0 ± 1.0 ms [37]) due to the differences in airway size which have a significant effect on the mode of diffusion (e.g., free diffusion vs. restricted) and amount of signal loss due to diffusion. **Table 1** shows T_2^* values obtained for hyperpolarized gas within rat lungs at 3 Tesla. As expected T_2^* estimates obtained for the major airways were smaller than the estimates observed in lung parenchyma.

2.3 Signal to noise ratio

An imaging sequence should be optimized to simultaneously ensure maximum SNR and minimal blurring in order to successfully perform high-resolution hyperpolarized ^{3}He MR measurements. Understanding of the mechanisms that affect SNR and contribute to image blurring is the basis for the developing an imaging technique appropriate for hyperpolarized gas imaging. Generally, an expression for the SNR of a FGRE sequence can be expressed as [42]:

$$SNR \propto \Delta x \Delta y \Delta z \sqrt{\frac{N_x N_y N_z}{BW_{read}}} f\left(\rho, \ P, \alpha, \ T_2^*, \ T_1, \ b, \ D\right) \tag{2}$$

where $\Delta x \Delta y \Delta z$ is the voxel size, $N_x N_y N_z$ is the number of k-space samples in each direction, BW_{read} readout bandwidth and $f(\rho, \ P, \alpha, \ T_2^*, \ T_1, \ b, \ D)$ is the pulse-sequence-dependent function that determines the signal amplitudes at read-out for the center of k-space [49]:

$$f(\rho, \ P, \ T_1, \ T_2^* \ \alpha, \ b, \ D) \approx \rho P \sin(\alpha) \exp^{(-TE/T_2^*)} \exp^{(-TR/T_1)} \exp^{(-b \ D)} \quad (3)$$

As it can be seen, the signal amplitudes at readout depend on the density (ρ) and polarization (P) of ³He, flip angle (α), TE, repetition time (TR) and finally, diffusion attenuation [50] introduced by slice select and/or frequency encoding gradients. In order to simultaneously minimize T_1 decay and T_2^*-induced blurring and maximize signal, one should use a short-TE (TE < 1 ms) center-out k-space traversal pulse sequence to ensure only density-weighting at the center of k-space. For the case of TE < T_2^*, and if the total acquisition time (1–10 s) is much less than T_1 (25–90 s) the pulse sequence dependent function can be expressed as:

$$f(\rho, \ P, \ \alpha, \ b, \ D) \approx \rho P \sin(\alpha) \exp^{(-b \ D)} \quad (4)$$

where b is the b-value, the diffusion weighting factor that depends on the diffusion gradient duration and magnitude (which in this case are imaging gradients); and D is the diffusion coefficient of ³He in the lung (0.1–2 cm²/s) [37, 50].

2.4 Flip angle

Let us consider each factor in Eq. (4) individually in order to optimize this function. As the hyperpolarized magnetization is not renewable due to the its non-equilibrium nature, it needs to be spent (flipped by RF pulses) very efficiently. A single 90° RF pulse can effectively waste all of the available magnetization. We start with the two approaches of setting flip angles in hyperpolarized gas MRI. The first method is the Constant Flip Angle (CFA) approach [51] or small flip angle approach (1° < flip angle <10°). Using a CFA approach, the optimal flip angle (α_{opt}), which provides the highest signal for sequential phase encode ordering, is expressed as [51]:

$$\alpha_{opt} = \tan^{-1}\sqrt{2/(N_y N_z)} \quad (5)$$

Unfortunately, the use of the optimal flip angle given by Eq. (5) leads to significant signal decay due to the constant-value RF pulses applied during k-space acquisition. As an example, for a 2D case where N_y = 128 and α_{opt} = 7.1° the signal decays by ~60% across the k-space). An undesirable consequence of such decay is reduced image resolution as result of the RF pulse "history" during k-space acquisition. Point-spread-function (PSF) simulations for a 2D case with center-out phase encode ordering (**Figure 1**) confirmed that the CFA approach leads to image blurring (Full Width at Half Maximum (FWHM) = 1.5 pixels) [47]. This signal decay-induced image blurring can be eliminated by using a Variable Flip Angle (VFA) approach (1° < flip angle <90°) [52]. VFA mitigates signal loss during image acquisition (i.e., blurring) by ensuring a constant signal for each phase-encode line by starting with a low flip angle and incrementing the flip angle of each RF pulse, line after line [52]. The flip angle for each ith phase-encode line of a VFA sequence can be calculated from the following equation [47]:

$$\alpha_i = \tan^{-1}\left[\frac{\exp\left(-(N_y N_z - i)TR/T_1\right)}{\sqrt{N_y N_z - i}}\right] \tag{6}$$

For the case where the total image acquisition time is much less than T_1 (T_1 typically >10 sec under normal conditions), Eq. (6) takes the simpler form [47]:

$$\alpha_i \approx \tan^{-1}\left[\frac{1}{\sqrt{N_y N_z - i}}\right] \tag{7}$$

For a 2D case (N_y = 128), α_1 = 5.1° and α_{128} = 90°, producing no CFA-like signal decay, and consequently, no image blurring due to RF pulse "history" [47]. Simulations have shown that VFA only shows blurring of 1.2 pixels due to discrete sampling [47] and because of these benefits this method is preferable for high spatial resolution ³He imaging.

2.5 *b*-Value

Eq. (4) suggests that signal decay due to diffusion is the main reason the MR signal degradation (assuming minimal T_1 and T_2^* induced blurring and signal loss) and consequently poses as the main difficulty for high spatial resolution ³He imaging. **Figure 2** shows the calculated NMR signal as a function of *b*-value for two different diffusion coefficients, typical for a small animal airways and lung parenchyma respectively [37]. It can be seen that for a *b*-value >3.5 s/cm², the signal intensity in the airway is almost zero and there is a 60% loss of signal for lung parenchyma. Let us consider the dependence of *b*-value on the diffusion gradient duration and magnitude. In general, the *b*-value for any gradient waveforms can be calculated from the first principles [42]:

$$b = \gamma^2 \int_0^{t_1}\left[\int_0^t G(t')\,dt'\right]^2 dt \tag{8}$$
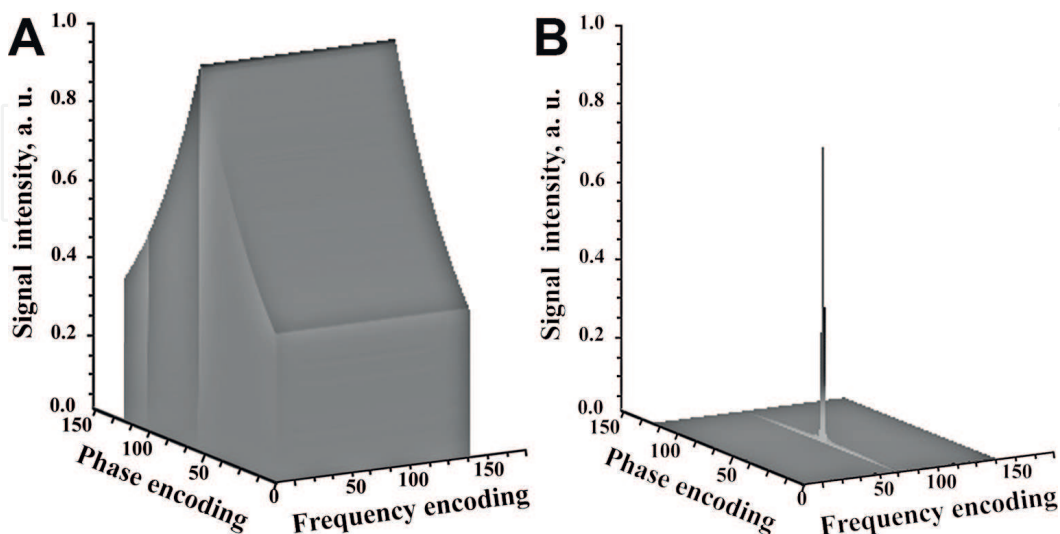

Figure 1.
Point spread function simulation for the CFA approach (a) the k-space is simulated for hyperpolarized CFA ³He signal of a 128 × 128 pixel object with α_{opt} = 7.12° (Eq. (5)) and infinite T_1. (b) Fourier transform of (a) revealing the PSF [47]. The calculated FWHM of the PSF indicates significant blurring (1.5 pixels) in the phase-encode direction [47]. The observed blurring is due to both RF pulse history of non-recoverable magnetization and discrete sampling [47]. Variable flip angle only shows blurring of 1.2 pixels due to discrete sampling [47]. Figure adapted from Ouriadov et al. [47].
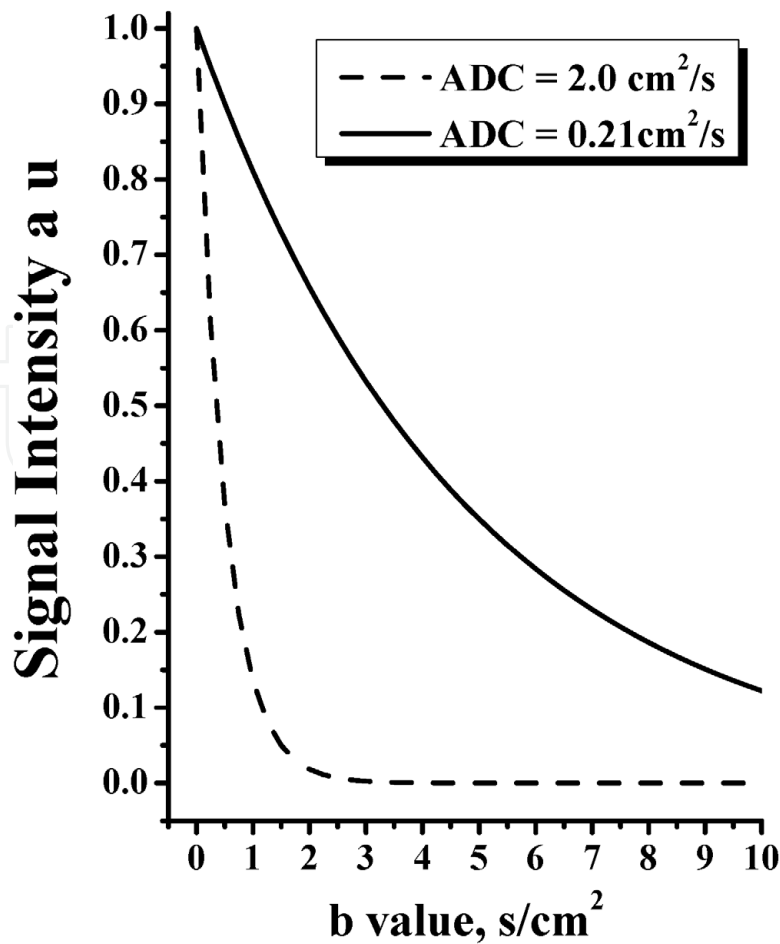
Figure 2.
Dependence of NMR signal on b-value for two different diffusion coefficients of ³He calculated from the diffusion term of Eq. (4). The dashed line curve represents signal obtained for a D value that is typical for airways (free diffusion) and the solid line curve represents signal obtained for a typical D value in lung parenchyma. Plot shows that for a b-value >3.5 s/cm², the signal intensity in the airway is almost zero and there is 60% of signal loss for lung parenchyma.

where γ is gyromagnetic ratio, G is gradient amplitude and t, t_1 is gradient duration. Unfortunately, Eq. (8) cannot be analytically simplified further for a gradient waveform specific to the frequency encoding imaging gradient. For a relatively simple diffusion gradient waveform such as two bipolar rectangular pulses, the b-value can be calculated based on the following equation [53]:

$$b = -\frac{2}{3}\gamma^2 G^2 \delta^2 t_d \text{ with } t_d = \left[\Delta - \frac{\delta}{3}\right], \quad (9)$$

where δ is the diffusion gradient duration, Δ is a distance between two gradient pulses and t_d is the diffusion observation time. Note, that b-value strongly depends on the gradient duration ($\delta^2 t_d = \text{time}^3$) then the magnitude ($G^2$), which suggests that minimizing the gradient duration reduces the b-value and consequently minimizes the signal loss. This is especially critical for high-resolution ³He imaging, as the imaging gradient magnitude cannot be really decreased when trying to achieve high spatial resolution, or small FOV for mice.

2.6 X-centric

As ³He gas has the highest self-diffusion coefficient of the usable hyperpolarized gases and it is a physical constant, the diffusion weighting b-value due to the application of frequency encoding gradient or x-gradient should be minimized as

much as possible. A full-echo FGRE pulse sequence ensures the highest b-value (and subsequent signal loss) for gradient echo based sequences [22, 25]. The use of a partial-echo (partial in the x-gradient direction, 62.5% sampled points) FGRE pulse sequence can significantly reduce the b-value compared to the full echo FGRE due to reduction in readout time; however, even this reduced b-value can be still large enough (>2.0 s/cm^2) to completely destroy MR signal in some lung geometries such as in the case of high spatial resolution ^{3}He imaging in small animals [22, 27]. The main limitation of FGRE is the undesirable dependence of the b-value on the x-gradient making this sequence not very suitable for high-resolution ^{3}He imaging. However, it is possible to modify the original FGRE sequence, so it ensures minimal b-values due to x-gradients and full independence of the b-value from the image resolution for the chosen field-of-view (FOV) and BW$_{read}$. A modified or X-Centric FGRE pulse sequence is presented in **Figure 3**. The idea of the X-Centric FGRE pulse sequence is straightforward. It acquires half of an echo in the x-direction by starting at the center of k-space then repeats the same k-space line but with the x-gradient inverted in order to collect the second half of the echo in x-direction. **Figure 4** shows part of an experimental x-gradient waveform (nominal resolution 78 μm) from the start of the line acquisition until the center of the k_x line for partial-echo (open squares and dashed line) and X-Centric (solid squares and solid line) FGRE pulse sequences. The area of the pre-phasing gradient shown on the plot is equal to area of the main readout gradient lobe for both acquisition methods. **Figure 4** suggests that the X-Centric FGRE should decrease b-value at k_x = 0 due to the much shorter diffusion time and smaller pre-phasing gradient magnitude lead-ing to higher signal at the center of k-space.

The X-Centric approach requires two discrete acquisitions for each k-space line making the method twice as long in acquisition time compared to a conventional partial-echo FGRE approach for a chosen spatial resolution and matrix size [17, 27, 39]. Though, this is not a significant cost to achieve high-resolution imaging of the lungs of small animals, the scan time can be further reduced by using a partial-echo method in the phase-encoding direction [17, 27, 39]. Note, that the use of a partial-echo method in the phase-encoding direction makes the X-Centric scan time only 10% longer than the partial-echo FGRE sequence for a similar spatial resolution and matrix size [27].
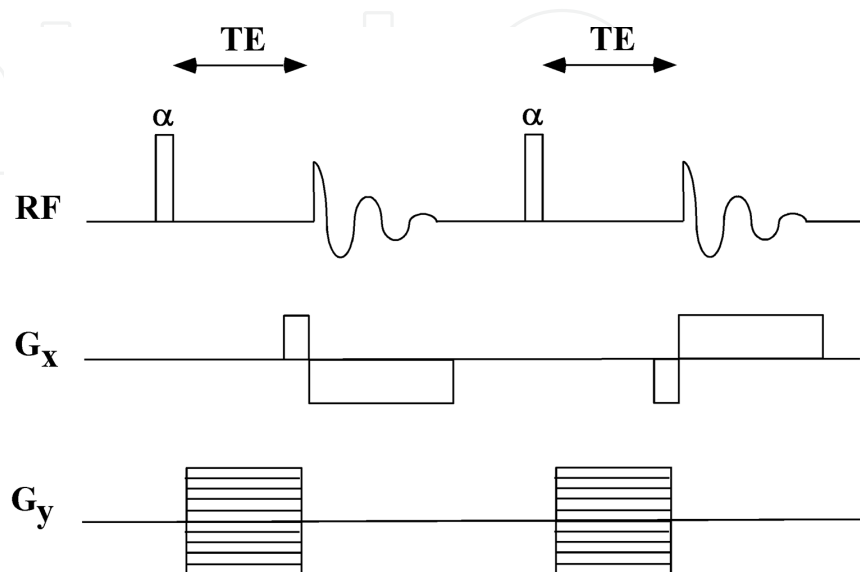

Figure 3.
Pulse sequence timing diagram of X-centric acquisition scheme. The X-centric approach minimizes signal loss due to diffusion since the number of k-space points acquired before the center of the k_x line is significantly reduced. Figure adapted from Ouriadov et al. [27].
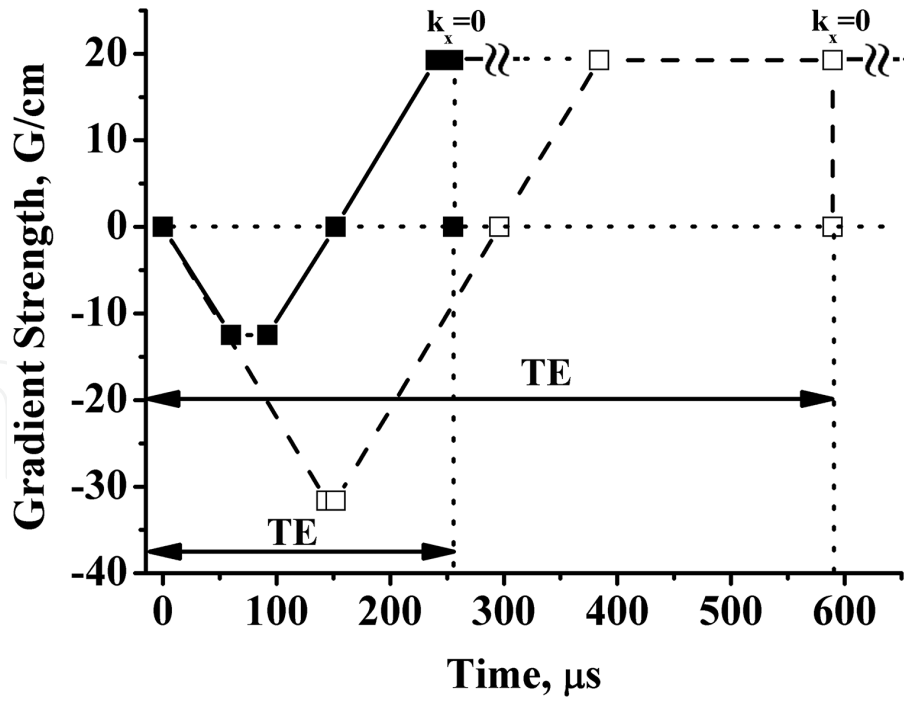
Figure 4.
Expanded view of the readout gradient waveform in partial-echo FGRE (open squares and dashed line) and X-centric (solid squares and solid line) for acquisitions with 256×256 image matrix FOV = 2×2 cm², and BW_{read} = 62.5 kHz [27]. X-centric waveform has a shorter TE (mainly determined by the duration of the phase-encoding gradient) and much smaller area compared to the partial-echo FGRE waveform resulting in a decreased b-value at k_x = 0 [27]. Both X-centric and FGRE gradient waveforms show the readout gradient until k_x = 0 point only [27]. Figure adapted from Ouriadov et al. [27].

2.7 Diffusion attenuation

The exact b-value for gradient waveforms presented in **Figure 4** can be calculated from Eq. (8). Thus, b-values calculated for the partial-echo and X-Centric FGRE (256×256 matrix size) were 2.29 and 0.061 s/cm² respectively. **Figure 2** indicates that a b-value more than 2.0 s/cm² leads to the complete signal decay in the major airway which is a significant limitation for high spatial resolution ³He imaging of the mouse lung. In contrast, the X-Centric sequence should theoretically ensure minimal signal decay for given diffusion coefficients. Note that for the unrestricted ³He diffusion case the theoretical SNR (SNR$_{theor}$) should depend only on b-value and D:

$$SNR_{theor} = S_0 \exp^{(-bD)} \tag{10}$$

where S_0 is the initial signal (S_0 = 1), D is the free ³He self-diffusion coefficient (2.0 cm²/s) and b takes on a value determined by the chosen FOV and BW$_{read}$.

According to Eq. (2), for the case of the high-resolution 2D ³He phantom imaging, the SNR should generally depend on the diffusion attention, image resolution, BW$_{read}$ and the first flip angle in the VFA scheme [27]:

$$SNR \propto P\rho \sin(\alpha_1) \, \Delta x \Delta y \sqrt{\frac{N_x N_y}{BW_{read}}} \exp^{(-bD)} \tag{11}$$

as Δx, Δy can be expressed through FOVs and N$_x$, and N$_y$ Eq. (11) can be rewritten as

9

$$SNR \propto P\rho \sin(\alpha_1) \ \frac{FOV_x FOV_y}{N_x N_y} \sqrt{\frac{N_x N_y}{BW_{read}}} \exp^{(-bD)} \tag{12}$$

If one keeps FOV, BW_{read}, ^{3}He polarization and volume constant across all phantom measurements, then the SNR comparison between the partial-echo and X-Centric FGRE can be done by normalizing the experimental SNR by the first flip angle in the VFA scheme (α_1) and matrix size ($\sqrt{N_x N_y}$). Thus, for a SNR normalized by the respective first applied flip angle and matrix size, one can write the following expression [27]:

$$SNR_{nor} = \frac{SNR}{\sin(\alpha_1)} \sqrt{N_x N_y} = Const \cdot \exp^{(-bD)} \tag{13}$$

where $Const = P\rho \ \frac{FOV_x FOV_y}{\sqrt{BW_{read}}}$. This final SNR_{nor} equation can be used for SNR comparisons of the phantom images obtained for different resolutions with the partial-echo and X-Centric FGRE methods; also this equation is similar to Eq. (10).

2.8 Phantom imaging

A plastic 10 mL syringe filled with hyperpolarized ^{3}He was used to validate the X-Centric sequence for high spatial resolution imaging [27]. **Figure 5** shows a 2D coronal view whole projection phantom images obtained for partial-echo (top panel) and X-Centric (bottom panel) FGRE for five different resolutions. Images start from 64 × 64 matrix size and end with 512 × 512 from left to the right [27]. The images indicate that at low nominal resolution (625 μm, 64 × 64 matrix size) there is no qualitative or visual difference in the SNR between the images obtained for the partial-echo and X-Centric FGRE. However, there is virtually no signal in phantom images obtained with partial-echo FGRE when nominal resolution is
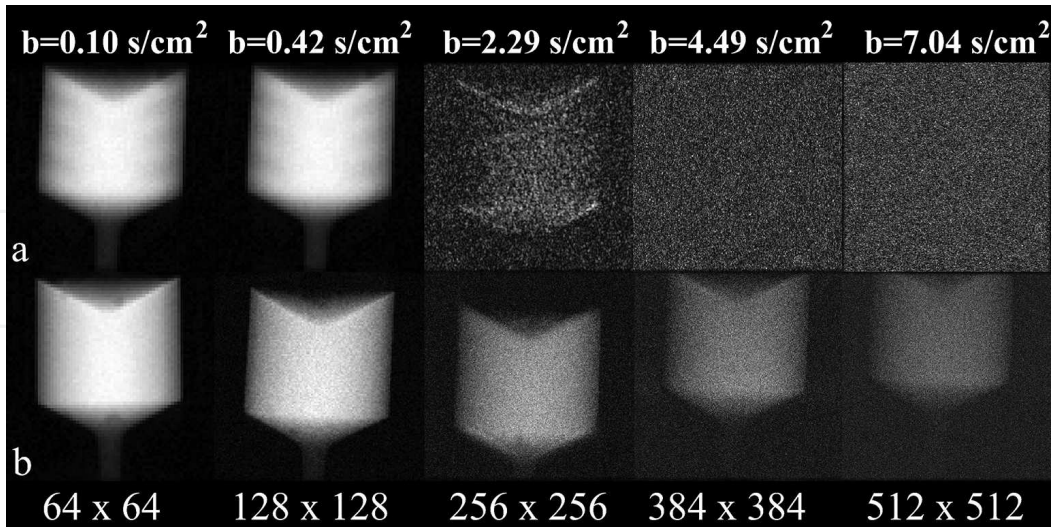
Figure 5.
Hyperpolarized ^{3}He phantom images (64 × 64, 128 × 128, 256 × 256, 384 × 384, 512 × 512 from left to right with a FOV = 2 × 2 cm^2, and BW_{read} = 62.5 kHz) obtained in the coronal plane at 1 atm gas pressure (D = 2.0 cm^2/s) for image acquisition times up to 6.7 s for: (a) partial-echo FGRE (top row with b-values ranging from 0.1 to 7.04 s/cm^2 at k_x = 0) and (b) X-centric (bottom row with a b-value equal to 0.061 s/cm^2 at k_x = 0) [27]. Whereas the X-centric images demonstrate only a gradual loss in signal intensity with increasing image matrix, the partial-echo FGRE had no signal intensity for images with matrix sizes of 384 × 384 and 512 × 512. The partial-echo FGRE image obtained for 256 × 256 has been filtered with a Hanning filter to increase signal intensity. The changes of syringe vertical position are due to the slight displacement of the syringe inside the holder between fresh gas administrations. Figure adapted from Ouriadov et al. [27].

greater than 256 × 256 (78 μm nominal resolution). As expected, the signal intensity of the images obtained with X-Centric gradually decays with increasing nominal resolution and decreasing flip angle (because the first pulse for VFA is a function of resolution, Eq. (7)) but even for 512 × 512 matrix size (39 μm nominal resolution) it does not go below the noise floor as is seen in the case of the partial-echo FGRE. The SNR_{nor} dependence on resolution (bottom axis) and/or b-value (top axis, partial-echo case only) for the phantom images obtained with the partial-echo (solid squares and solid line) and X-Centric FGRE (solid circles and solid line) is plotted in **Figure 6**. Clearly, the SNR_{nor} obtained for the X-Centric did not depend on image resolution, i.e., diffusion attenuation was minimal even for very high image resolution (39 μm). The experimental phantom results were consistent with the predicted SNR (SNR_{theor}) calculated based on Eq. (10) for the partial-echo (open squares and dashed line) and X-Centric FGRE (open circles and dashed line). Eqs. (10) and (13) indicate that for the case of unrestricted ³He diffusion (D = 2 cm²/s) one should observe minor signal loss (∼10%) using X-Centric and almost 100% signal loss using the partial-echo FGRE for a nominal resolution greater than 78 μm. Thus our consideration of the factors determining the SNR for high spatial resolution ³He MR measurements shows that in the case of relatively short TR and TE (pulse sequence parameters for 256 × 256 matrix size are present in **Table 2**) diffusion is the major reason for signal loss. Using the X-Centric method, diffusion decay due to the x-gradients is significantly minimized. It should be noted that we observed a slight
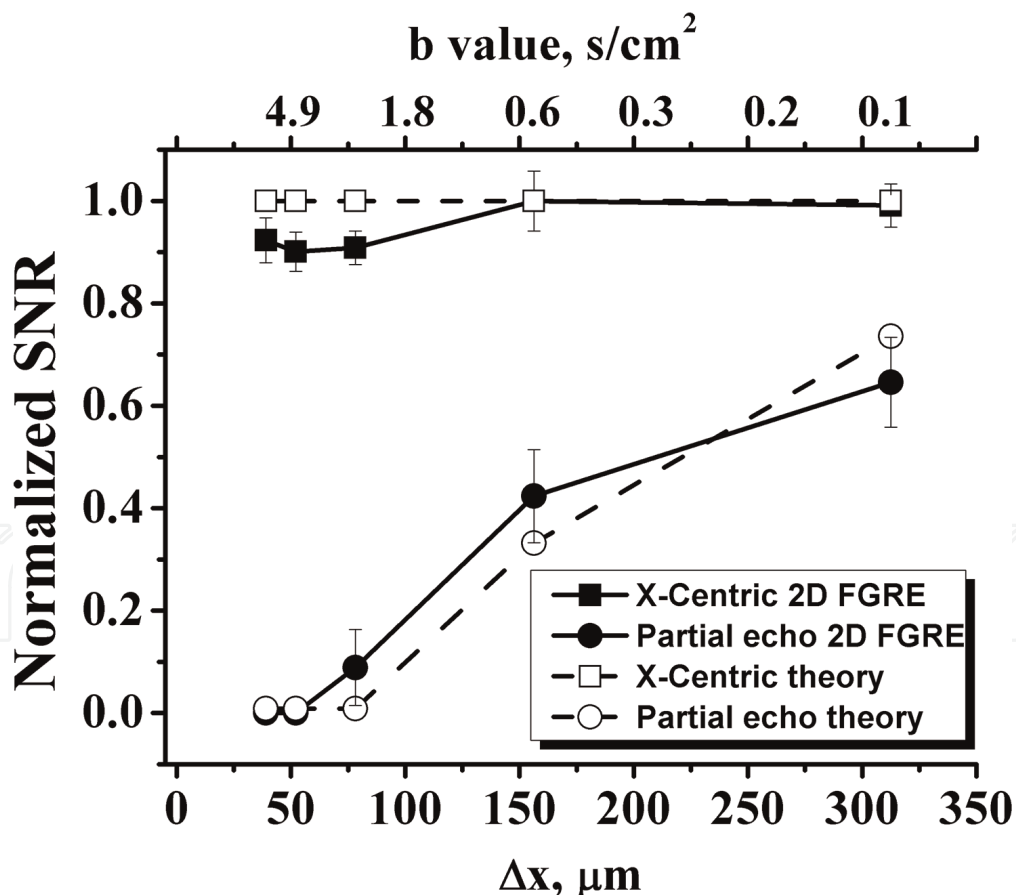

Figure 6.
Scaled normalized SNR of the phantom images (Eq. (13)) shown in Figure 5a and b versus spatial resolution (bottom horizontal axes) and b-value (top horizontal axes) for: (i) partial-echo FGRE (solid circles and solid line) and X-centric (solid squares and solid line) acquisitions [27]. These data are consistent with the predicted data (open squares and dashed line for partial-echo and open circles and dashed line for X-centric) based on the calculated b-values (Eq. (13)) [27]. This plot shows independence of normalized SNR from image resolution for the x-centric acquisition schemes [27]. The b-value axis (calculated for experimental x-gradient waveform based on Eq. (8)) applies only to the partial-echo FGRE curves as the b-values for X-centric curves were constant (0.061 s/cm²) as a function of resolution [27]. Figure adapted from Ouriadov et al. [27].

	³He MRI	**¹²⁹Xe MRI**	**¹⁹F MRI**
TE/TR (ms)	0.70/3.7	0.81/50.0	.50/4.0
Flip angle	3.2° (VFA)	6.4° (CFA)	70 ° (EA)
FOV (mm²)	20 × 20	250 × 250	60 × 60
Matrix size	256 × 160	128 × 80	64 × 40
Number of averages	1	1	60
Slice orientation	Axial/coronal	Axial/coronal	Axial/coronal
Pixel size (mm³)	0.078 × 0.078	1.9 × 1.9 × 300	0.94 × 0.84
Scan time (s)	1.1	>8	>10
MRI scanner	GE 3 T MR750	Philip. 3 T Achieva	Philip. 3 T Achieva

VFA = variable flip angle; CFA = constant flipped angle; EA = Ernst angle; FOV = field of view; TR = relaxation time; TE = echo-time.

Table 2.
MRI acquisition parameters for methods in this chapter.

decrease of the SNR$_{nor}$ (around 10%) for a nominal resolutions better than 75 μm (**Figure 6**) which were likely due to T_2^* decay because as resolution increases, TE becomes longer due to the longer duration of phase-encoding gradient. Nevertheless, X-Centric phantom images show no evidence of image blurring due to the RF pulse history or T_2^*-based signal decay in the frequency/phase encoding directions. The phantom measurements have confirmed that significant diffusion attenuation induced by the x-gradient with the partial-echo FGRE sequence can be the main restriction for high spatial resolution ³He imaging of the lung.

3. High spatial resolution imaging of mouse lung

3.1 Animal preparation

The animal protocol was approved by the Animal Use Subcommittee of the University Council on Animal Care at the University of Western Ontario, London, Ontario, Canada and the Animal Care Committee at Merck Frosst Canada, Kirkland, Quebec, Canada. Each mouse (BALB/c) was pretreated with Midazolam (1 mg/kg) intraperitoneally (i.p.) 5 min before anesthesia with ketamine (95 mg/kg, i.p.) and xylazine (6.4 mg/kg, i.p.). Following anesthesia, the tail vein was cannulated (26 GA Abbott catheter) to maintain anesthesia with ketamine (30 mg/kg) and xylazine (2 mg/kg) every 40 min. To allow artificial mechanical ventilation, the trachea was cannulated by tracheotomy using an 18 GA Teflon catheter. A line for administration of pancuronium (0.8 mg/kg, i.p.) was established using a 26 GA cannula to allow for injections after the mouse was being ventilated inside the scanner. Other physiological instrumentation included ECG and a rectal temperature probe (SA Instruments Inc., Stony Brook, NY).

3.2 Ventilation

It was a very challenging task to design a ventilator to ventilate mice inside an MRI because of the restrictions due to the high magnetic field environment and the requirement to accurately deliver very small tidal volumes of gas to the lungs of mice at a high ventilation rate. Under spontaneous breathing, the mouse maintains its oxygenation with a tidal volume less than 0.1 ml [54, 55]. Because of the dead

space volume within the tubing necessary for connecting mouse airways to the ventilator, the mouse was normally ventilated with tidal volume of 0.2 ml (8 ml/kg). In this range, the amount of the ventilating gas (or fresh gas) getting compressed in the gas line could significantly reduce the portion of fresh gas entering the lungs for gas exchange. Without a proper correction for this effect, adequate ventilation would not be achieved at this ventilating setting. In many cases, the ventilation was set with a much larger tidal volume (>10 ml/kg) at a slower ventilation rate (60–90 bpm). Since lung volume under spontaneous breathing is only 0.3–0.4 ml [56], the larger tidal volume approach could overextend the airways. As a result, many mice were observed to expire shortly after the ventilation, impeding the completion of studies.

To resolve these problems, we modified a flexiVent ventilator (**Figure** 7, Scireq, Montreal, QC, Canada) that incorporated real-time monitoring of volume and pressure to allow corrections of the gas compression effect. To minimize the gas line volume and ensure the effectiveness of ventilation, a non-metal swing valve was designed and placed close to the animal (inside the scanner) to regulate the gas flow. Different than the pneumatic valves normally used in the magnetic environment, the swing valve was connected to two driving solenoid valves (which reside far away from the high magnetic field) via two multiple-section light-weight carbon fiber rods. This mechanical design enabled fast open/close activations. The activation of a solenoid valve pulls the swing valve to close the ports on one side and open the ports on the other side. Two solenoid valves were activated in sequence to generate a swing motion that opens and closes the ports on the respective sides alternately. This swing motion was synchronized with the plunging motion of the piston that drives the gas into the lung to form a ventilation cycle. Because of the fast response of the swing valve, the modified flexiVent ventilator is capable of performing the forced oscillation method to access pulmonary mechanics. To minimize oxygen-induced depolarization (T_1 decay) of hyperpolarized ³He gas, the flexiVent ventilator was modified to deliver breathing gas and hyperpolarized ³He gas separately using two individual syringes. The ventilation system was integrated to the MR scanner (**Figure** 7) using custom-designed LabView software (National Instruments) to allow ventilation-synchronous acquisition. Following the animal preparation, the animal was connected to the ventilator and ventilated using a tidal volume of 8 ml/kg at 100 bpm and was placed inside the scanner. The breath-hold time for imaging was 1 s.

Figure 7.
GE 3 T clinical MRI scanner using an external gradient set for rodents and the integrated custom-built flexiVent ventilator for mice.

3.3 ^{3}He polarization and delivery

^{3}He gas was polarized using an optical pumping spin-exchange system (Helispin™, GE Healthcare, Durham, NC). The ^{3}He gas was typically polarized for at least 8 hours to achieve a polarization over 35%. Prior to transferring the hyperpolarized ^{3}He gas to a 150 mL Tedlar bag (Jensen Inert Products, Coral Springs, FL), the bag was carefully washed with N_2 gas three times to eliminate any oxygen contamination. Following the gas filling, the ^{3}He bag was placed inside a custom-made plexiglass chamber and connected to a ^{3}He intake line of the ventilator. The chamber was then placed within the homogenous B_0 field inside the scanner to conserve ^{3}He polarization (T_1 = ~43 min). To facilitate gas intake by the ventilator, the pressure in the chamber was kept at 3 cm-H_2O during the gas delivery.

To validate the X-Centric imaging method, 2 mL at 1 atm of the hyperpolarized ^{3}He gas was drawn into a 10 mL syringe for phantom testing [27].

3.4 MRI hardware and sequence parameters

Hyperpolarized ^{3}He MR imaging was performed on a GE clinical scanner (3 T, Excite 12.0) which was converted using a home-made insert gradient set (**Figure 8**, maximum gradient at 50 G/cm, 17 cm in diameter, slew rate = 2100 mT/m/s) [43] to allow high spatial resolution imaging for mice. This high performance insert gradient set was used for phantom and mouse imaging [27]. A quadrature birdcage RF coil for mice (**Figure 9**, 3 cm in diameter and 6 cm in length, Morris Instruments, Ottawa, ON) was used for ^{3}He imaging (97.3 MHz) [27]. The coil was driven using a 8 kW AMT 3 T90 RF power amplifier (GE Healthcare, Waukesha, WI)

Figure 8.
High performance water cooled insertable gradient set with maximum gradient at 50 G/cm, 17 cm in diameter and slew rate = 2100 mT/m/s used for high-resolution ^{3}He imaging.
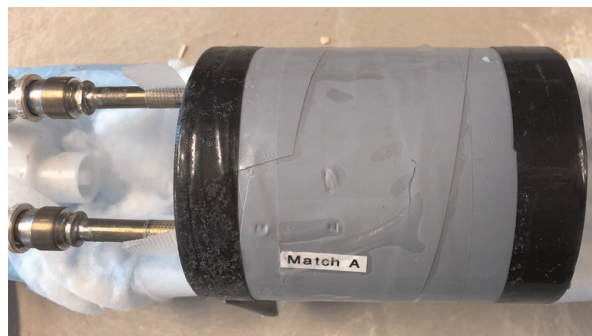

Figure 9.
A quadrature birdcage RF coil for mice (Morris instruments, Ottawa, ON): 97.3 MHz, 3 cm in diameter and 6 cm in length, was used for used for high-resolution ^{3}He imaging.

using a manufacturer-supplied T/R switch and preamplifier tuned to 97.3 MHz. Typical rectangular 90° RF pulse lengths were 100 μs [27]. A VFA RF pulse trajectory was employed to reduce blurring due to RF de-polarization [47, 52]. Center-out sampling in the phase-encoding direction was used [52]. The VFA pulses were calibrated as described in [48].

3.5 Image reconstruction

A custom-made IDL6.4 (ITT Visual Information Solutions, Boulder, CO) routine was used for off-line Fast Fourier transformation (FFT) of the k-space data. For reconstruction of the X-Centric data, a combination of both halves of k-space was applied prior to the inverse Fourier transformation as follows. To form a full line of k-space data in the read-out direction, the two half-echo data sets were combined [17]. Each half-echo data set included two additional points (BW_{read} = 62.5 kHz dwell time was 8 μs) prior to k_x = 0 which can be thought of as partial-echo factor of 0.505 for each half.

Acquisition of a few extra k_x data points is helpful since the presence of background gradients can shift the origin of k-space by one or more points resulting in mis-sampling or causing image artifacts [57]. These extra k-space points (only two) were removed before combining the two halves of k-space prior to reconstruction [17]. The disadvantage of this approach is that this leads to a b-value three times larger and longer TR due to the extra sampled points. However, phantom results demonstrate that this increased b-value (b = 0.061 s/cm^2) is still quite practical, ensuring minimal mis-sampling even in the presence of significant background-gradients and gradient-induced eddy currents [17, 27, 39]. Collection of the extra four k_x points (two points per half) for each k_x line results in a 1.5% over-sampling factor for a 256 × 256 matrix size as an example [27].

3.6 In-vivo imaging

X-Centric sequence parameters for the highest image resolution (78 μm) are shown in **Table 2**. *In-vivo* high-resolution 2D whole lung projection ^{3}He mouse lung images obtained for partial-echo (top panels) and X-Centric (bottom panels) FGRE acquisitions for three different matrix sizes are shown in **Figure 10** (axial view) and **Figure 11** (coronal view). Images were obtained during a 1 s breath-hold following three wash-out ^{3}He pre-breaths. It is easy to see that both the axial and coronal images of the mouse lung obtained at high spatial resolution (78 μm) with X-Centric demonstrates visible signal in the major airways. Axial and coronal images of mouse lung obtained for the same resolution setting with partial-echo FGRE show no signal in the trachea as well as lower SNR in the lung periphery. The mean SNR for X-Centric images computed from the mouse lung airways and parenchyma [58] were 25 and 14 respectively [27]. The corresponding mean SNR for the partial-echo FGRE computed for airways and parenchyma were 1.8 (which is less than the Rose criteria of SNR = 5, [59]) and 8 respectively [27]. The large b-value of the partial-echo FGRE led to complete signal destruction in the major airways where ^{3}He experiences near-free diffusion (D = 2 cm^2/s). Besides this, a relatively long TE (1.2 ms [27]) in combination with a shorter T_2^* (**Table 1**) in the mouse lung trachea also significantly contributes to signal decay together with diffusion losses. In comparison to the larger airways, the lung parenchyma within the images obtained with partial-echo FGRE still shows some signal, which is not surprising considering that the ^{3}He diffusion was significantly restricted here (D = 0.21 cm^2/s [37]) and T_2^* value was long enough (**Table 1**).

Figure 10.
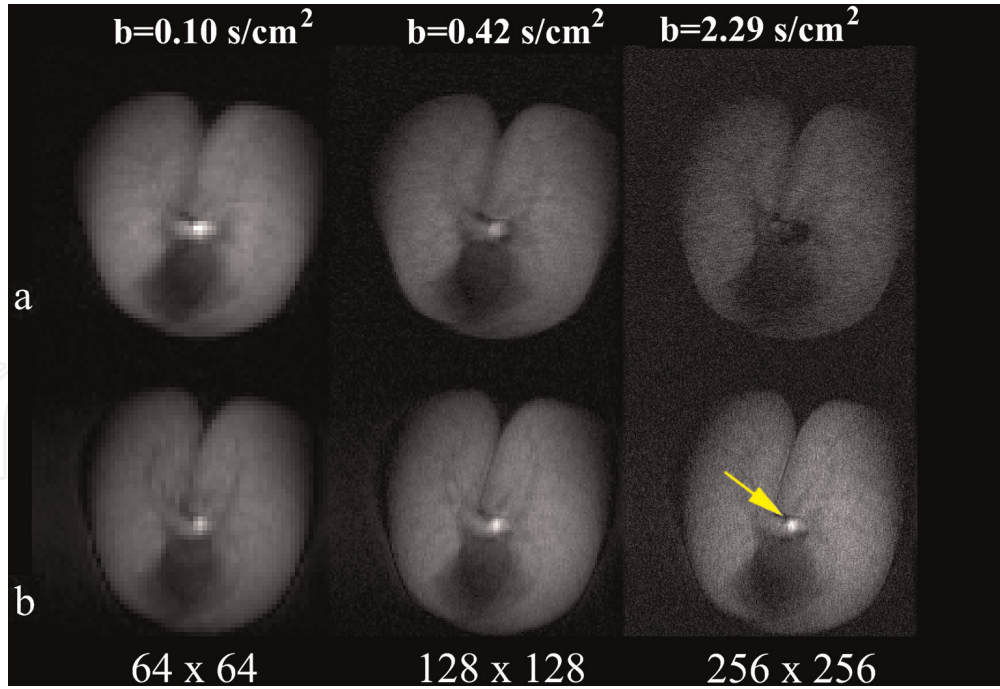*Hyperpolarized ^{3}He mouse images (64×64, 128×128, 256×256 from left to right FOV = 2×2 cm^2, and BW$_{read}$ = 62.5 kHz) obtained in the axial plane using a single breath hold with image acquisition times up to 1.1 s for: partial-echo FGRE (top panel, b-values ranging from 0.1 to 2.29 s/cm^2 at k_x = 0) and X-centric (bottom panel, b-value equals 0.061 s/cm^2 at k_x = 0) [27]. At high-resolution (256×256), the partial-echo FGRE images show no signal intensity in the trachea in contrast with the high-resolution X-centric images due to differences in the incidental diffusion weighting in the large airway compared to the lung parenchyma (shown by the arrow) [27]. Figure adapted from Ouriadov et al. [27].*

The larger SNR in the major airway (X-Centric mouse lung images) compared to the lung parenchyma is likely due to the higher ^{3}He density in trachea and reasonably short TE used in X-Centric sequence (0.7 ms [27]).

It is useful to calculate the SNR efficiency (Υ) of the X-Centric and partial-echo FGRE acquisitions was using the following equation [60]:

$$\Upsilon = \frac{SNR/(\Delta x \Delta y)}{\sqrt{T_{scan}}} \qquad (14)$$

where T_{scan} is the total imaging time (in s) and SNR was measured based on the mean of Region of Interests (ROI) placed in the rodent lung airways and parenchyma divided by the standard deviation measured in the background (noise) [58]. Thus, X-Centric was 13.4 times more efficient than the partial-echo FGRE sequence for the case of the major airways [27] and 1.7 times more efficient in case of MR imaging of parenchyma [27] (**Figure 11**).

3.7 Limitations

One of the limitations of the X-Centric method is the need to use the FFT for image reconstruction from two half-echo k-space samples rather than a single k-space. Instead, one can use a single half-echo k-space and Partial Fourier Reconstruction (PFR) [61]. To test this idea we used the Projection Onto Convex Sets (POCS) method [62] to reconstruct a phantom image for 130×256 ($2 + 128 \times 256$) matrix size (**Figure 5b**). **Figure 12** shows phantom images obtained with PFR (left column) and FFT (right column) for three different matrix sizes. The following SNR values were obtained for the presented images: SNR = 39 (160×256, PFR); SNR = 54 (160×256, zero-filling in x-direction and then FFT); SNR = 45
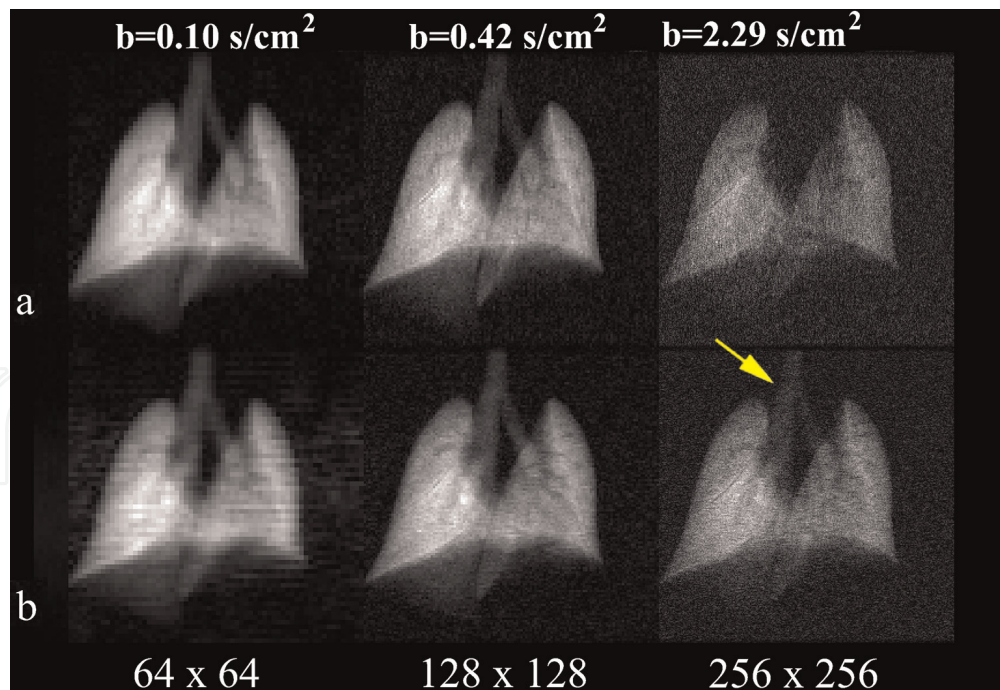
Figure 11.
Hyperpolarized ³He mouse images (64 × 64, 128 × 128, 256 × 256 from left to right FOV = 2 × 2 cm², and BW$_{read}$ = 62.5 kHz) obtained in the coronal plane within a single breath hold with image acquisition times up to 1.1 s for: partial-echo FGRE (top panel, b-values ranging from 0.1 to 2.29 s/cm² at k$_x$ = 0) and X-centric (bottom panel, b-value equals 0.061 s/cm² at k$_x$ = 0) [27]. At high-resolution (256 × 256), the partial-echo FGRE images show no signal intensity in the trachea in contrast with the high-resolution X-centric images due to differences in the incidental diffusion weighting in the large airway compared to the lung parenchyma (shown by the arrow) [27]. Figure adapted from Ouriadov et al. [27].

(130 × 256, PFR); and SNR = 58 (256 × 160, zero-filling in y-direction and then FFT). The results confirm that the FFT with zero-filling approach gives better SNR than the PFR method for 160 × 256 matrix (39 vs. 54). We have calculated the efficiency of half-echo acquisition (130 × 256, SNR = 45) reconstructed with PRF and X-Centric (256 × 160, 62.5% under-sampling in y-direction, SNR = 58) reconstructed with FFT in order to compare imaging methods. Thus, the calculated efficiency ratio is 0.87 (Eq. (14), with T_{scan} = 256 and 160 + 160 y-gradient steps for the half-echo and the X-Centric respectively). This shows that a half-echo acquisition is 13% less efficient than X-Centric, which reflects smaller SNR due to the 50.1% sampling vs. 62.5% sampling for the case of X-Centric, but half-echo acquisition is ~200 ms faster due to the doubling of y-gradient steps for X-Centric. We believe that our half-echo acquisition vs. X-Centric results indicate that the half-echo approach is 20% faster but 10% less SNR efficient than X-Centric. A structured phantom needs to be used for probing the potential smoothing effects and resolution implications following the Partial Fourier Reconstruction.

3.8 Future role of X-Centric

The focus of this chapter is a presentation of a fast and SNR efficient imaging method for high spatial resolution imaging of mouse lungs that include both the airways and lung parenchyma. Such a technique can be potentially used for mapping the morphological changes and ventilation heterogeneity associated with rodent models of asthma or ovalbumin-challenged model (OVA). **Figure 13** shows an example of ventilation heterogeneity maps obtained for a sham mouse (right column) and OVA treated mouse (left column). The figure compares increased (a and c) and decreased (b and d) ventilation heterogeneity indexes from a sham mouse (left column) and an OVA mouse (right column) under similar increases in
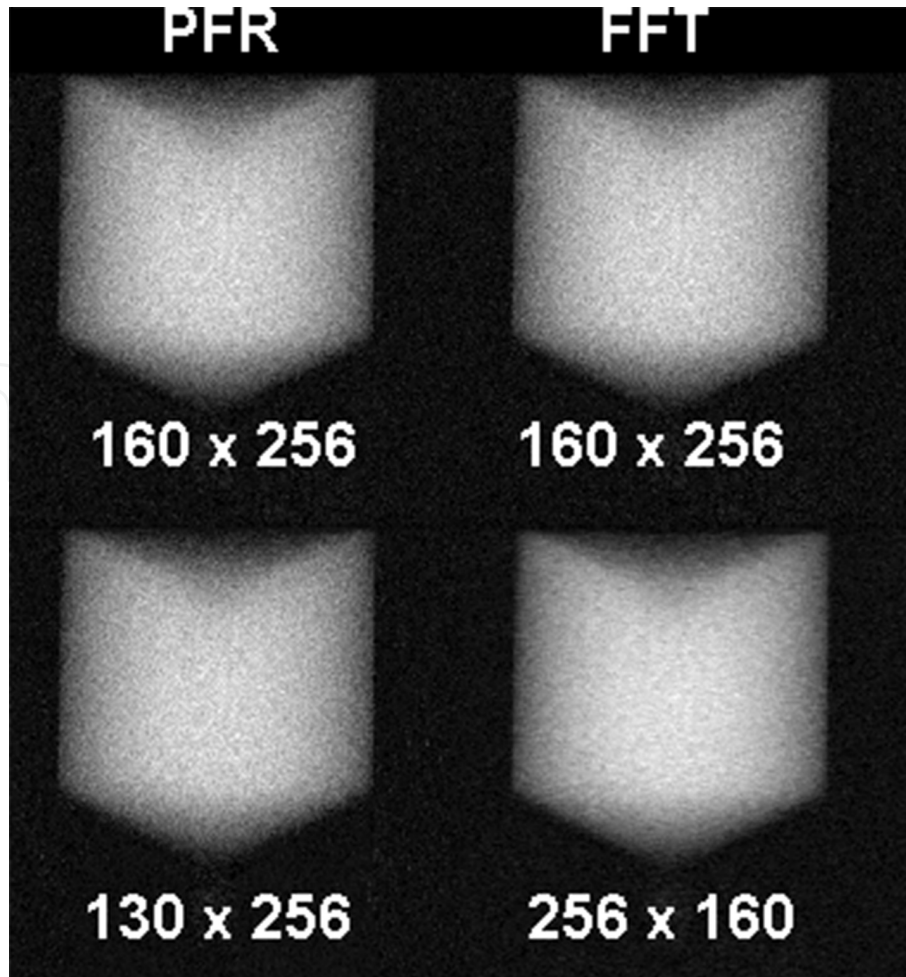
Figure 12.
Phantom images obtained with partial Fourier reconstruction (PFR, left column) and fast Fourier reconstruction (FFT, right column) for three different matrix sizes are shown. The open source partial Fourier reconstruction (projection onto convex sets (POCS), 2013) was obtained from the official MatLab web site. The following signal-to-noise ratio (SNR) values were obtained for the presented images: SNR = 39 (160 × 256, PFR); SNR = 54 (160 × 256, FFT); SNR = 45 (130 × 256, PFR); and SNR = 58 (256 × 160, FFT).

airways resistance (104% vs. 93%, respectively) and elastance (21% vs. 27%, respectively). The white and red lines in the figure outline the lung contour before and after the Methacholine inhalation (MCh) challenge, respectively. Airway resistance and tissue elastance were measured immediately following each scan. Lung images were then analyzed using local standard deviation (SD) in sliding (9 × 9 pixels^2) ROIs. The ventilation heterogeneity index (*VHI*) was given by:

$$VHI\ (\%) = \frac{SD_{post-MCh} - SD_{pre-MCh}}{SD_{pre-MCh}} x100\%\tag{15}$$

The post-MCh lung function data were normalized by the pre-MCh values to give the percent change. The sham mouse and an OVA mouse data are shown only as an example of the potential X-Centric pre-clinical application. However, data suggested that ventilation heterogeneity following MCh challenge may be commensurate with traditional lung function testing to access the airway hyper-responsiveness in the OVA mouse model. The observed heterogeneity in ventilation distribution could potentially provide a novel endpoint to study disease modification in asthma, as well as for better diagnosis and classification of asthma in the clinic.

The X-Centric method described here should also be beneficial for clinical hyperpolarized lung MRI and other applications where short-TE techniques are
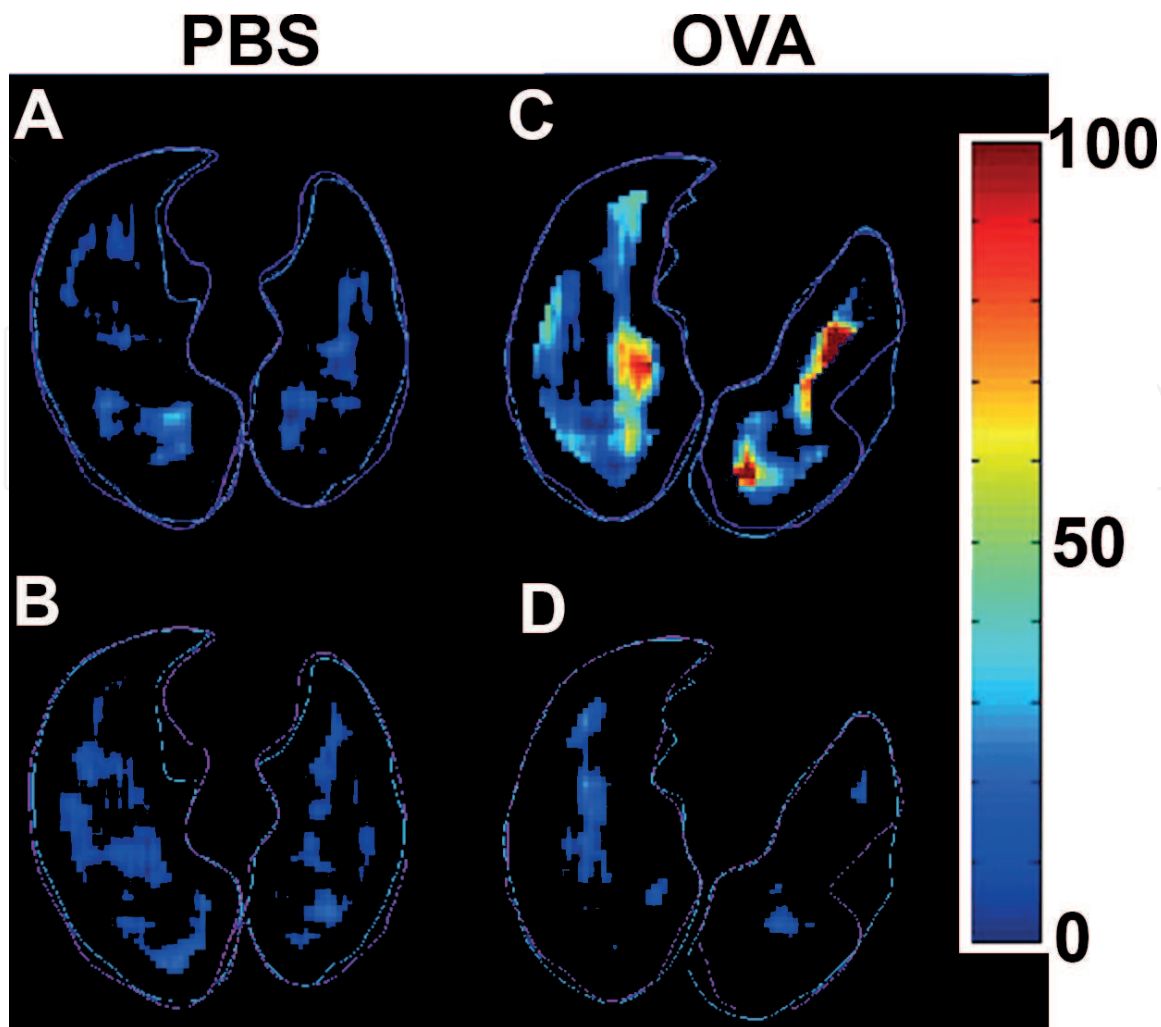
Figure 13.
The VHI *maps from a sham mouse (left column) and an OVA treated mouse (right column). The white and red lines in the figure outline the lung contour before and after the Methacholine inhalation challenge, respectively. We applied partial-echo FGRE to acquire a 96 × 48 matrix and zero-filled in phase-encoding direction to get a 96 × 96 matrix using FOV = 2 × 2 cm², BW$_{read}$ = 83.3 kHz, TE = 0.42 ms and TR = 1.3 ms. the scan time for each image was ∼ 100 ms and the calculated* b-*value was ∼0.7 s/cm². The mouse was ventilated at 100 breaths/min and 8.5 ml/kg tidal volume using a ventilation pattern consisting of 160 ms of inhalation, 120 ms of breath-hold (for image acquisition) and 320 ms of exhalation. A series of ³He MR lung images (every 15 s) were acquired before and after methacholine inhalation challenge (160 μg/kg, IV).*

needed. **Table 2** helps to estimate the acquisition time for BW$_{read}$ = 62.5 kHz and FOV = 200 × 200 mm² (pediatric study [63]) for two matrix sizes frequently used in human studies [6]: 128 × 128 × 14 slices and 256 × 256 × 14 slices (3D case) yielding resolutions of 3.1 × 3.1 × 15 mm³ and 1.6 × 1.6 × 15 mm³ at FOV = 400 × 400 × 15mm³. With the assumption of partial sampling in the phase-encoding direction and taking into account that the maximum strength of the clinical gradient system is typically 4–5 G/cm with a maximum slew rate of 200 T/m/s [6], one can calculate the acquisition to be around 5 s for a 128 × 128 matrix and 16.7 s for a 256 × 256 matrix. As the 256 × 256 matrix at a FOV of 20 × 20 cm² corresponds to 781 μm nominal resolution, this should lead to 70% signal decay in airways due to diffusion-weighting according to [22] for the case of full-echo FGRE. The X-Centric approach could eliminate 90% of the signal loss due to incidental diffusion-weighting in the major airways. Parallel imaging approaches [64] or compressed sensing approaches [65, 66] can also speed up data acquisition even more and are a straight-forward extension of the X-Centric approach described here.

Until now, X-Centric has not been used in any pediatric studies; nevertheless, hyperpolarized gas MRI is gradually becoming an important research tool, allowing
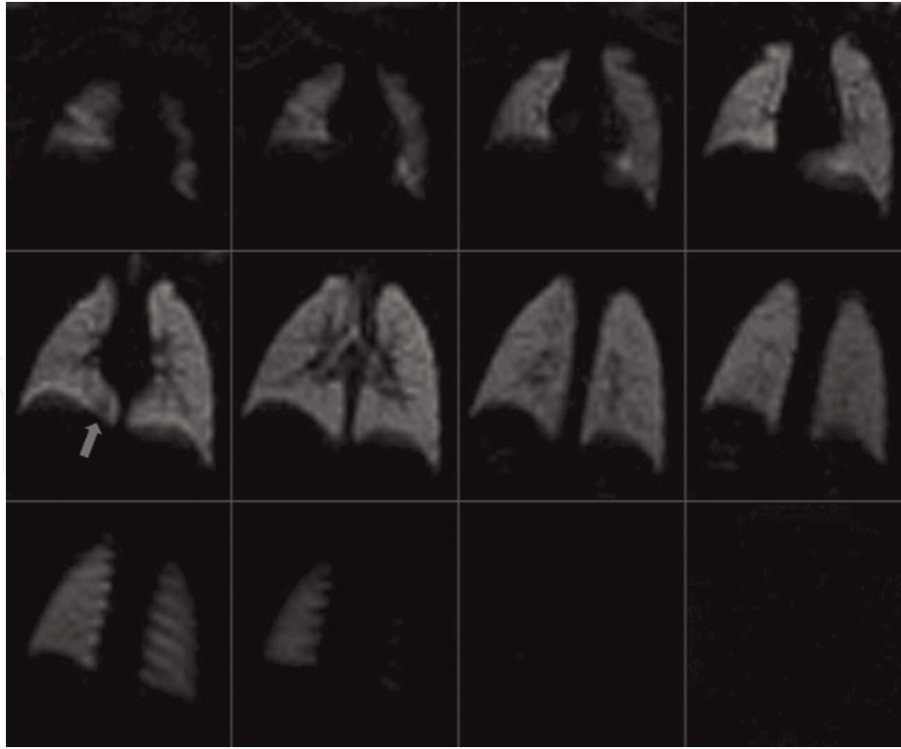
Figure 14.
³He coronal MR images of a 17-month-old non-sedated, unrestrained infant with Cystic Fibrosis. Homogeneous ventilation is seen throughout the lungs. A possible tiny ventilation defect is seen at the right base (arrow). No noticeable motion artifacts are noticeable. 15 spiral interleaved acquisitions (TE = 0.9 ms, TR = 8.1 ms, pixel size = 3 × 3, number of slices = 18; slice thickness = 10 mm, and FOV = 40 × 40 cm²). Adapted from Altes et al. [28].

for longitudinal observation of lung diseases in children such as Cystic Fibrosis (CF). **Figure 14** shows ³He MRI lung images obtained from a 17-month old patient with CF. Note, the regions of hypo-intensity are difficult to see at this resolution, but using X-Centric, one should be able to gain diagnostic value and better enhance the contrast in these regions. We believe that X-Centric can be very useful for not just CF but the longitudinal observation of other lung diseases like Bronchopulmonary Dysplasia (BPD). Abnormal prematurity at birth (<28 weeks gestation) frequently requires neonatal intensive care and mechanical ventilation due to respiratory distress syndrome due to limited or lack of lung surfactant and incomplete lung development. Ventilator-associated lung injury, along with the extreme prematurity of the lungs themselves, causes abnormal and irregular lung growth (BPD) [67]. The relatively short signal life-time caused by the need to scan newborns inside their neonatal incubators (causing B_0 field distortions, especially at high field) and also the need for smaller FOV make the X-Centric approach ideally suitable for high-resolution neonatal lung MRI.

4. Use of X-centric with other MR-visible nuclei

4.1 Gas phase ¹²⁹Xe MRI

³He is a rare and expensive isotope (**Table 1**), so a worldwide clinical translation of the ³He MRI method is quite questionable, especially when there is a relatively inexpensive alternative—¹²⁹Xe MRI. In contrast to the ³He isotope, the ¹²⁹Xe isotope is much more abundant (∼26% natural abundance) and cost efficient (**Table 1**). In addition, recent improvements in the xenon polarization process have enabled sufficient increase in the level of ¹²⁹Xe polarization (>30%) and production volume

of the polarized gas (~2 L per hour) [68, 69]. Presently, ^{129}Xe lung MRI is translating towards a clinical tool, and it has recently been used as a clinical tool (along with ^{3}He MRI) in the United Kingdom [70]. The North-American xenon consortium [71] expects ^{129}Xe MRI to be the Food and Drug Administration approved in the first quarter of 2020.

Presently, the main directions of ^{3}He MRI are pediatric and neonatal studies (using relatively small doses of ^{3}He) mainly due to the cost of the ^{3}He isotope and the high quality of the ^{3}He lung images. In turn, ^{129}Xe MRI is much more suited for adult lung imaging; however, the low SNR of ^{129}Xe images (compared to ^{3}He) impede the development of many novel acquisition schemes that are highly sensitive to SNR [72], such as isotropic voxel static-ventilation imaging and accelerated multiple *b*-value diffusion-weighting MRI [73]. Mentioned above, recent improvement in xenon polarization [68, 69] provides a way to develop advanced imaging methods previously not possible. This is especially critical for investigations in patients with asthma and COPD. Here we report the isotropic-voxel, high-resolution 3D ^{129}Xe static-ventilation image acquired in a single 16 s breath-hold, with the necessary and sufficient SNR to quantify ventilation defect percent [74] estimates (an efficient asthma and COPD biomarker). To the best of our knowledge, a voxel size of $3 \times 3 \times 3$ mm^3 is the highest currently achieved resolution for ^{129}Xe human lung images. **Figures 15** and **16** show the axial and coronal lung images obtained for a healthy volunteer using an isotropic voxel 3D FGRE pulse sequence. The central slice SNR was around 30 for both axial and coronal view images. The gas phase of ^{129}Xe has a relatively low free diffusion coefficient (0.14 cm^2/s in air,
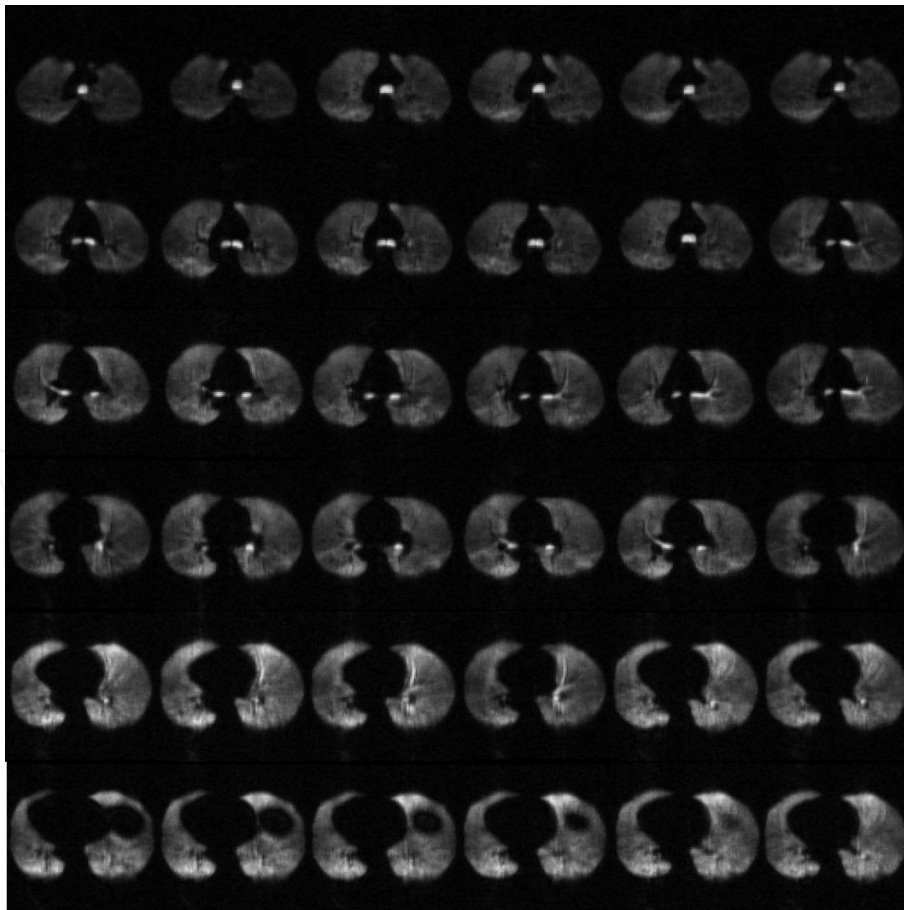

Figure 15.
Axial view isotropic ^{129}Xe MRI static-ventilation slices from superior to inferior for a healthy volunteer. Isotropic-voxel ^{129}Xe static-ventilation images were acquired using an axial plane 3D fast gradient-recalled Echo sequence (TE/TR/initial-flip-angle = 1.3 ms/4.0 ms/0.9°, variable-flip-angle, reconstructed matrix size = 128 × 128 × 104 [axial view], pixel bandwidth = 217 Hz, and FOV = 40 × 40 × 32 cm³, voxel size = 3 × 3 × 3 mm³). ^{129}Xe lung images by and courtesy of G. Parraga.
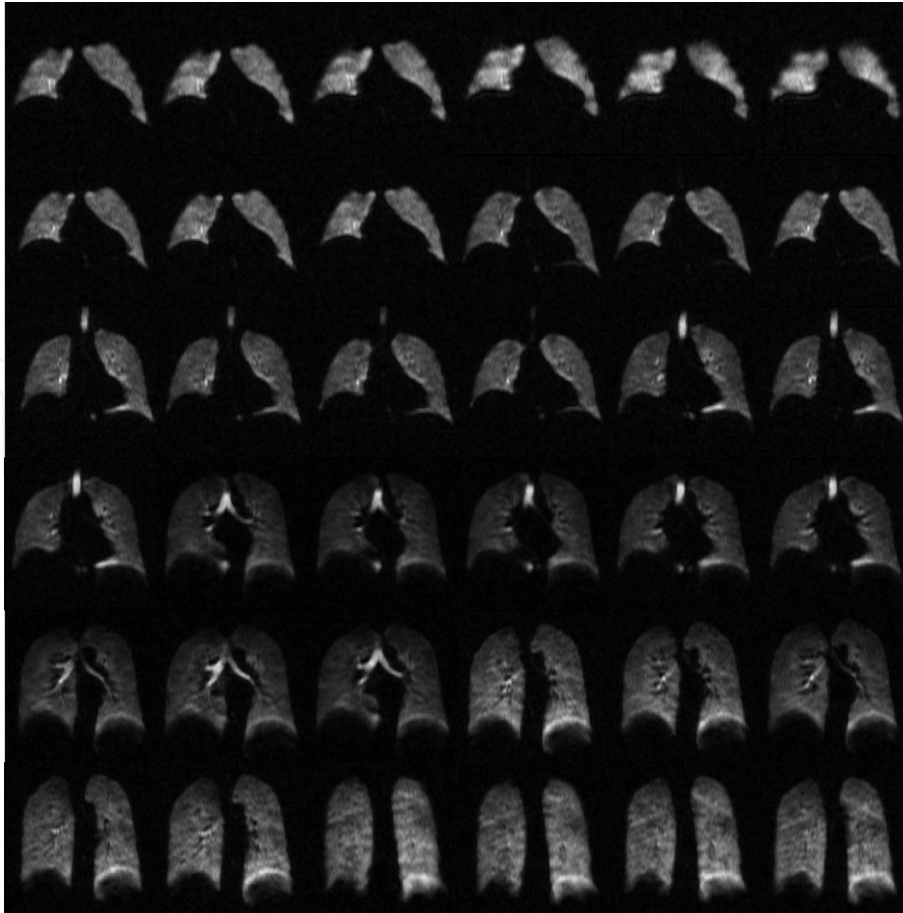
Figure 16.
Coronal view isotropic ^{129}Xe MRI static-ventilation slices from anterior to posterior for a healthy volunteer. Isotropic-voxel ^{129}Xe static-ventilation images were acquired using an axial plane 3D fast gradient-recalled Echo sequence (TE/TR/initial-flip-angle = 1.3 ms/4.0 ms/0.9°, variable-flip-angle, reconstructed matrix size = 128 × 128 × 104 [axial view], pixel bandwidth = 217 Hz, and FOV = 40 × 40 × 32 cm³, voxel size = 3 × 3 × 3 mm³). ^{129}Xe lung images by and courtesy of G. Parraga.

Table 1) and relatively long signal life-time (10–30 ms depends on the field strength [75]), so the benefits of the X-Centric approach (overcoming a high diffusivity and short T_2^*), may not be very obvious for the case of healthy subjects compared to the traditional FGRE sequence. However, lungs of patients with severe emphysema, COPD (smokers or ex-smokers), BPD and Alpha-1 Antitrypsin Deficiency may show regions with significant terminal airways destruction, changing the diffusion regime to nearly-free diffusion (xenon $D \approx 0.22$ cm^2/s when mixed 50/50 with helium-4 [6]) in such regions, naturally leading to substantial local reduction of T_2^* (up to 50% reduction due to the fast motion through the local B_o inhomogeneities within the lung airspaces) [73] especially at high field. X-Centric, is a short-TE method that should be able to better visualize lung regions with short T_2^*; and therefore, a better tool for helping to make clinical decisions and for therapy planning.

4.2 Dissolved phase ^{129}Xe MRI

Unlike its counterpart ^{3}He, ^{129}Xe is highly soluble in a variety of solvents and biological materials, and exhibits a large range of chemical shifts within these distinct chemical environments (Ostwald solubility coefficients of 0.17 [40]). Of particular interest is dissolved phase ^{129}Xe residing in and exchanging with lung tissue (tissue barrier) and red blood cells (RBC) [76–78]. The exchange can be measured using MRI and it is also possible distinctly resolve and quantify ^{129}Xe within the

tissue barrier and RBC. Exploiting these signals for diagnostic imaging purposes can be difficult since for example, only about 2% of inhaled xenon dissolves into the tissue barrier and RBC [76, 79], and the corresponding T_2^* values are often short (~2 ms) [80]. There is an urgent need for efficient short-TE methods to acquire these short T_2^* signals and enable deeper study of a number of lung abnormalities such as ventilation/perfusion mismatch [81, 82] and of other organs including xenon brain perfusion imaging [72, 83] and imaging of the xenon-encapsulated Cryptophane-A functionalized with anti-cancer drugs [84].

The feasibility of the X-centric method was initially demonstrated using ³He for high-resolution rat lung imaging [39] indicating its ability to overcome diffusion induced signal attenuation within the trachea and substantially reducing TE and t_d as well as the magnitude of the imaging gradient [27]. The low diffusivity and low gyromagnetic ratio of ¹²⁹Xe (**Table 1**) suggest that diffusion decay due to the imaging gradients would not be an obstacle for high-resolution ¹²⁹Xe gas MRI; however, the relatively short T_2^* of the dissolved xenon remains a problem, as it leads to signal decay and contributes to image blurring simultaneously. Clearly, short-TE pulse sequences such as spiral [85, 86] or X-Centric [17, 27] are absolutely necessary to acquire images of xenon dissolved in lung tissue and blood.

Figure 17b shows dissolved phase hyperpolarized xenon obtained from within a water-filled resolution phantom (**Figure 17a**) on a clinical 3 T MRI scanner (maximum gradient strength was 5 G/cm, sequence parameters are shown in **Table 2**). The ¹²⁹Xe image shows that X-Centric can be used to image dissolved phase xenon efficiently (within a breath-hold) and with reasonable signal-to-noise ratio (SNR = 12). After reconstruction, the smallest geometric features of the resolution phantom in the X-Centric image are discernable (yellow arrows). It should be noted, that the available SNR achievable when imaging dissolved phase ¹²⁹Xe principally depends on concentration, polarization and relaxation times and even physiological parameters such as blood flow and blood oxygenation. The quality of the polarizer, solubility of the solvents used and chemical environments all play a role. Nevertheless, techniques employing significant reductions in echo-times can deliver higher SNR than is typically achievable for spins within environments where their transverse relaxation times are significantly shortened. Though, the phantom dissolved-phase spins had estimated T_2^*-values of roughly 20 ms, the potential for using X-Centric for imaging xenon within the tissue barrier, RBC and
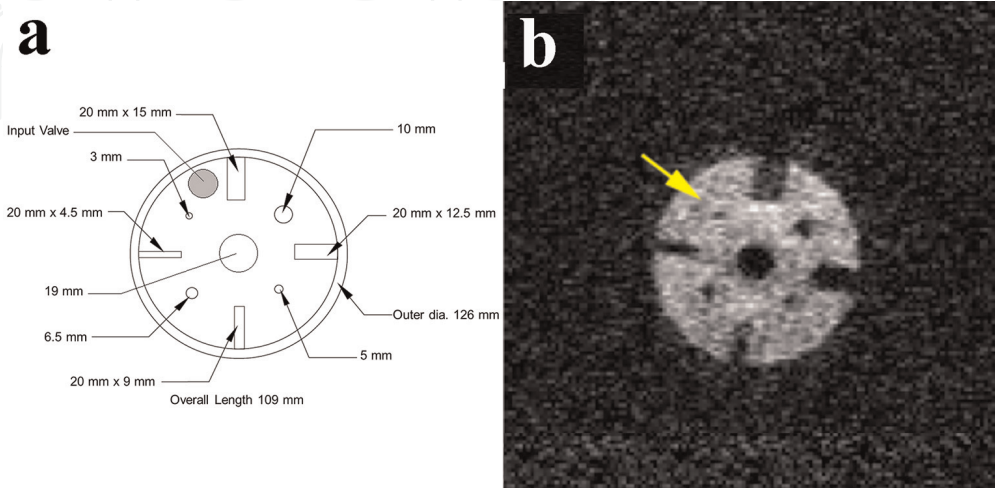

Figure 17.
*Resolution phantom (a) and (b) ¹²⁹Xe X-centric image obtained in a clinical 3 T MRI scanner. Signal-to-noise ratio value was 12.5. The yellow arrow indicates the 3 mm diameter feature of the resolution phantom demonstrating resolution of the smallest feature of the phantom. The X-centric sequence parameters are shown in **Table 2**. Adapted from Ouriadov et al. [17].*

brain ($T_2{}^* < 2$ ms) is high and the prospects for high-resolution dissolved phase imaging (currently not available) are demonstrated.

4.3 Static-ventilation ^{19}F MRI

The limited use of the hyperpolarized ^{3}He/^{129}Xe MRI imaging modality can be partially explained by its need for utilizing expensive isotopes and polarizers, the latter requiring specially-trained personnel. Inert inhaled fluorinated gas MRI can be a promising and less expensive (**Table 1**) alternative to hyperpolarized ^{3}He/^{129}Xe MRI. ^{19}F MRI does not require the use of rare isotopes (100% naturally abundant, **Table 1**) or expensive polarizers. ^{19}F gases (such as perfluoropropane (C_3F_8) and sulfur hexafluoride (SF_6) [17, 18]) can be imaged using high field (≥ 1.5 T) clinical MRI scanners; however, a multi-nuclear amplifier and receiver along with RF coils tuned to the ^{19}F frequency are still required [18, 19]. Fluorine-19 has a large gyromagnetic ratio ($\sim$95% of ^{1}H, **Table 1**), both SF_6 and C_3F_8 have several ^{19}F atoms per molecule, and have relatively short T_1 values making these highly attractive options for researchers (**Table 1**, [87]). Short T_1 translates to overcoming their low thermal polarization [17, 88] values by rapid signal averaging. Additionally, because it is not hyperpolarized, Fluorine-19 gases can be mixed with O_2 without polarization losses, preserving the image quality patient safety simultaneously during a breath-hold scan [89]. Inert fluorinated gases have very short $T_2{}^*$ values ($T_2{}^* < 2$ ms [87]), therefore imaging methods with short echo times are preferable. As we demonstrated previously, the X-Centric acquisition can be reliably used for phantom and *in-vivo* measurements using both ^{3}He and ^{129}Xe gases. Similar to the dissolved ^{129}Xe case, a short apparent transverse relaxation time specific to the fluorinated gas can potentially lead to fast signal attenuation and image blurring. As X-Centric is a short-TE sequence it should be able to ensure sufficient SNR of the fluorinated gas images, and also minimal image blurring. **Figure 18a** and **b** show an SF_6 high-resolution phantom (**Figure 14a**) and rat lung images obtained using X-Centric on a clinical 3 T MRI scanner (maximum gradient strength was 5 G/cm, *in-vivo* image sequence parameters are shown in **Table 2**). *In-vivo* data acquisition was synchronized to breath-hold durations using the ventilator [17]. Rat lungs were saturated with an SF_6/O_2 80/20 gas mixture during 3 min of normal free breathing at a breathing rate of 60 breaths/min. After 3 min, the fluorinated gas/O_2 mixture was suspended followed by a 10 sec breath-hold to obtain *in-vivo* rat lung image (**Figure 18b**) [17]. Inert fluorinated gas images confirm that X-Centric ensures
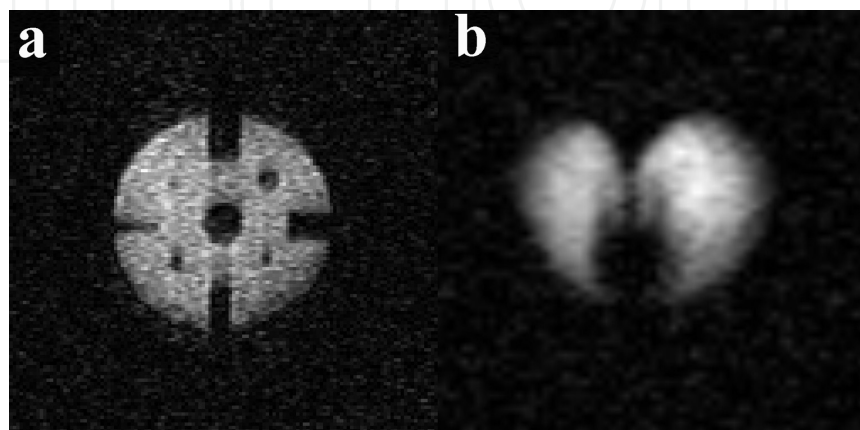

Figure 18.
*(a) An SF_6-filled resolution phantom image (FOV = 20 × 20 cm², BW_{read} = 200 Hz/pixel) obtained using X-centric (TE = 0.5 ms, SNR = 14) and (b) in-vivo ^{19}F X-centric rat lung image obtained in a clinical 3 T MRI scanner. SNR values were 14 and 40 respectively. ^{19}F X-centric sequence parameters are shown in **Table 2**. Figure adapted from Ouriadov et al. [17].*

sufficient SNR (14 and 40 for the phantom and *in-vivo* images respectively) and resolution (phantom images shows all details) of fluorinated gas images, when apparent transverse relaxation time is less than 2 ms. These results suggest the possibility for translating these techniques directly to human use because they are demonstrated using a clinical scanner using clinical gradient coils.

4.4 Dynamic ^{19}F MRI

^{19}F gas MRI also has a high potential for successful dynamic lung imaging [88, 90] due to the fact that fluorinated gases can be mixed with O_2 which helps to restore the initial magnetization faster (decreasing T_1), in contrast to the hyperpolarized gases. Furthermore, imaging times are shortened and breath-holds are more easily tolerated by the patients [89]. A technique like this permits the acquisition of regional fractional-ventilation [23, 48, 91] which can be very useful as a radiation free alternative to CT for detecting gas trapping in lung diseases such as lung fibrosis and COPD [88]. Recently, free-breathing ^{19}F (C_3F_8) dynamic lung imaging has been demonstrated in human lungs [89]. **Figure 19** (top panel) shows the gradual wash-out ^{19}F gas within the ^{19}F MRI lung images obtained from a COPD patient for eight wash-out breaths [89]. As expected, each new wash-out breath of air replaced some volume of the fluorinated gas in lung, so the signal intensity of the resulting images was gradually attenuated. The following equation can be fitted to this wash-out data [48]:

$$S(n) = S_0 \cdot (1 - r)^n \qquad (16)$$

where S_0 is the initial signal, n is the breath number, $S(n)$ is the signal intensity after a certain number of wash-out breaths and r is the fractional-ventilation parameter [17, 48]. In turn, r can be expressed as the fraction between new ^{19}F incoming to lung, and the total volume of ^{19}F (V_{total}) [17, 48]:

$$r = \frac{V_{new}}{V_{total}} = \frac{V_{new}}{V_{old} + V_{new}} \qquad (17)$$

where V_{new} and V_{old} are the "new" and "old" gas volumes in each voxel at each breath. In general, Eq. (16) can be approximated with the stretched exponential (or Kohlrausch) function [92]:
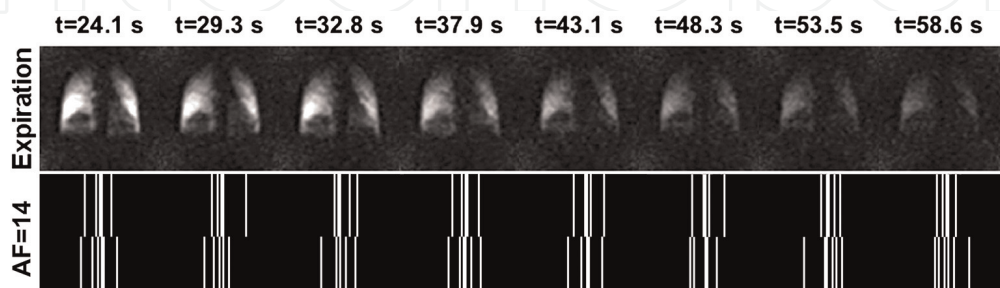

Figure 19.
Corresponding ^{19}F gas washout in expiration for one section of the three-dimensional volume (top panel). ^{19}F washout was started at 24.6 s. Images were acquired using a coronal plane 3D spoiled gradient-Echo sequence (TE/TR/flip-angle = 1 ms/3 ms/5°, matrix size = 192 × 130 × 88, pixel bandwidth = 550 Hz, and FOV = 50 × 37.5 × 35.2 cm³, voxel size = 2.6 × 2.9 × 4 mm³) with a generalized auto-calibrating partially parallel acquisition with a reduction factor of 2 in a single breath-hold. Figure adapted from Gutberlet et al. [89]. Sparsity pattern for AF = 14 (bottom panel) depicting the k-space under-sampling scheme, ensuring a variety of sparsity patterns for each time point or wash-out breath. AF = accelaration factor.

$$S(n) = \exp\left[(-nr)^{\beta}\right] \tag{18}$$

where $0 < \beta \leq 1$, and r is the fractional-ventilation. This simple function has been recently used to combine the CS method with under-sampling in the parametric direction [93], which permitted an acceleration factor (AF) of 7 in multi b-value diffusion-weighted ^{3}He MRI measurements [73]. Generally, a reasonable choice of the AF value depends on a number of the images in parametric direction. The main idea behind this relationship is to keep the reconstruction errors low [93]. As we stated above in this chapter, X-Centric is Cartesian pulse sequence, which can be naturally used for under-sampling in imaging (phase-encoding) and parametric (time) directions following CS with the stretched exponential method [93]. To our knowledge this is first record of the possibility of using CS combined with the stretched exponential method for dynamic lung imaging studies. **Figure 19** (bottom panel) shows an under-sampled X-Centric k-space pattern ensuring AF = 14. Remarkably, this means that only 8% of k-space, or five k-space lines (out of 64) are sampled to achieve a "full dataset" and each image in time can be acquired 13 times faster, which obviously helps to avoid the motion artifacts common to free-breathing data acquisition. Additionally, X-Centric can potentially ensure a much shorter TE compared to the spoiled gradient-echo sequence (TE = 1 ms) used to obtained ^{19}F human lung images [89]. Retrospective X-Centric-like under-sampling of the ^{19}F dynamic rat lung *in-vivo* data (64 × 64 matrix size, nine wash-out images [17]) available to us has confirmed that AF = 14 led to less than a 12% reconstruction difference (pixel-by-pixel comparison between the fully-sampled image and one reconstructed from the retrospectively under-sampled k-space). Therefore, the choice of X-Centric for dynamic ^{19}F gas MRI lung imaging will speed up imaging time and improve image quality making it an optimal choice for this kind of imaging.

The remaining obstacle preventing wide-spread high-resolution ^{19}F MRI with or without X-Centric is the generally low SNR of ^{19}F lung images. In this particular case, the further improvement of the image quality strongly depends on a hardware component, specifically from RF coil systems. It has been recently demonstrated that the use of a multi-channel phased-receive array can significantly improve the image quality of the ^{19}F MRI lung images [94]. This is a very promising result suggesting that the combination of the X-Centric method with advanced array-type RF coil system will permit future high-resolution ^{19}F MRI human lung imaging in both static-ventilation and dynamic studies.

5. Conclusion

In summary, hyperpolarized ^{3}He X-Centric MR imaging with high spatial resolution was proven to be a robust technique in phantom and mouse lung measurements yielding a nominal resolution of 39 μm and 78 μm respectively. In particular, mouse major airways with less restricted diffusion of ^{3}He ($D \sim 0.9$ cm^2/s) could only be visualized with the X-Centric method. Note, that the high nominal resolution (78 μm) in *in-vivo* scans was achieved within 1 s breath-hold. These results suggest that the X-Centric method can potentially fill a gap and need for high spatial and temporal resolution imaging method for the small model of asthma studies.

Another beneficial feature of the X-Centric sequence is the significantly reduced echo-time, so the method can be used for imaging of nuclei with short signal lifetimes such as hyperpolarized ^{129}Xe dissolved within the lung tissue barrier and/or

Red Blood Cells, and inert fluorinated gas (SF$_6$) inside the lungs. In both cases the $T_2{}^*$ value is less than 2 ms. The feasibility and future potential of short-TE X-Centric-based X-Nuclei measurements were demonstrated using ^{129}Xe dissolved in water as well as SF$_6$ within rat lungs.

Acknowledgements

The authors would like to thank the following individuals for assistance with MRI experiments and data analysis: Grace E. Parraga, Giles E. Santyr, Mitchell S. Albert, Marcus J. Couch, Tao Li and Iain K. Ball. A special thanks to Ben T. Chen for providing support for the hyperpolarized ^{3}He gas, animals, and ventilator.

Conflict of interest

The authors do not have any conflict of interest.

Notes/thanks/other declarations

We thank Michael Völker for providing the MatLab code (Projection onto Convex Sets (POCS), 2013) for image reconstruction. We thank Abascal et al. for providing the MatLab code (Signal Decay Into the Reconstruction (SIDER), 2017) for image reconstruction.

Nomenclature

AF	acceleration factor
BW$_{read}$	bandwidth
BALB/c	laboratory-bred strain of the house mouse
BPD	bronchopulmonary dysplasia
C$_3$F$_8$	perfluoropropane
CF	cystic fibrosis
CFA	constant flip angle
COPD	chronic obstructive pulmonary disease
D	self-diffusion coefficient
^{19}F	fluorine-19
FFT	fast Fourier transformation
FGRE	fast gradient recalled echo
FOV	field of view
FWHM	full width at half maximum
GE	general electric
^{1}H	hydrogen-1
^{3}He	helium-3
MCh	methacholine inhalation challenge
MRI	magnetic resonance imaging
O$_2$	oxygen
OVA	ovalbumin-challenged model
PFR	partial Fourier reconstruction
POCS	projection onto convex sets

RBC	red blood cells
ROI	region of interest
RF	radio frequency
SD	standard deviation
$SD_{post-MCh}$	post-methacholine challenge SD
$SD_{pre-MCh}$	pre-methacholine challenge SD
SF6	hexafluoride
SNR	signal to noise ratio
SNR_{nor}	normalized signal to noise ratio
SNR_{theor}	theoretical signal to noise ratio
T_1	longitudinal relaxation time
$T_{1,0}$	T_1 expected in the absence of O_2
T_2^*	apparent transverse relaxation time
T_{scan}	total scan (imaging) time
TE	echo time
T/R	transmit and receive
TR	repetition time
VFA	variable flip angle
VHI	ventilation heterogeneity index
^{129}Xe	xenon-129

Author details

Matthew S. Fox[1,2] and Alexei V. Ouriadov[1,2]*

1 Lawson Health Research Institute, London, ON, Canada

2 Department of Physics and Astronomy, Western University, London, ON, Canada

*Address all correspondence to: aouriado@uwo.ca

IntechOpen

References

[1] Albert MS, Cates GD, Driehuys B, Happer W, Saam B, Springer CS, et al. Biological magnetic resonance imaging using laser-polarized 129Xe. Nature. 1994;**370**(6486):199-201

[2] Saam BT, Yablonskiy DA, Kodibagkar VD, Leawoods JC, Gierada DS, Cooper JD, et al. MR imaging of diffusion of 3He gas in healthy and diseased lungs. Magnetic Resonance in Medicine. 2000;**44**(2):174-179

[3] Salerno M, de Lange EE, Altes TA, Truwit JD, Brookeman JR, Mugler JP 3rd. Emphysema: Hyperpolarized helium 3 diffusion MR imaging of the lungs compared with spirometric indexes—Initial experience. Radiology. 2002;**222**(1):252-260

[4] Swift AJ, Wild JM, Fichele S, Woodhouse N, Fleming S, Waterhouse J, et al. Emphysematous changes and normal variation in smokers and COPD patients using diffusion 3He MRI. European Journal of Radiology. 2005;**54**(3):352-358. DOI: 10.1016/j.ejrad.2004.08.002

[5] Evans A, McCormack D, Ouriadov A, Etemad-Rezai R, Santyr G, Parraga G. Anatomical distribution of 3He apparent diffusion coefficients in severe chronic obstructive pulmonary disease. Journal of Magnetic Resonance Imaging. 2007;**26**(6):1537-1547. DOI: 10.1002/jmri.21205

[6] Kirby M, Svenningsen S, Owrangi A, Wheatley A, Farag A, Ouriadov A, et al. Hyperpolarized 3He and 129Xe MR imaging in healthy volunteers and patients with chronic obstructive pulmonary disease. Radiology. 2012;**265**(2):600-610

[7] Altes TA, Powers PL, Knight-Scott J, Rakes G, Platts-Mills TA, de Lange EE, et al. Hyperpolarized 3He MR lung ventilation imaging in asthmatics: Preliminary findings. Journal of Magnetic Resonance Imaging. 2001;**13**(3):378-384. DOI: 10.1002/jmri.1054

[8] de Lange EE, Altes TA, Patrie JT, Gaare JD, Knake JJ, Mugler JP 3rd, et al. Evaluation of asthma with hyperpolarized helium-3 MRI: Correlation with clinical severity and spirometry. Chest. 2006;**130**(4). DOI: 1055-62. DOI 10.1378/chest.130.4.1055

[9] Tzeng YS, Lutchen K, Albert M. The difference in ventilation heterogeneity between asthmatic and healthy subjects quantified using hyperpolarized 3He MRI. Journal of Applied Physiology (Bethesda, MD: 1985). 2009;**106**(3): 813-822. DOI: 10.1152/japplphysiol. 01133.2007

[10] Fain SB, Gonzalez-Fernandez G, Peterson ET, Evans MD, Sorkness RL, Jarjour NN, et al. Evaluation of structure-function relationships in asthma using multidetector CT and hyperpolarized He-3 MRI. Academic Radiology. 2008;**15**(6):753-762. DOI: 10.1016/j.acra.2007.10.019

[11] Svenningsen S, Eddy RL, Lim HF, Cox PG, Nair P, Parraga G. Sputum eosinophilia and magnetic resonance imaging ventilation heterogeneity in severe asthma. American Journal of Respiratory and Critical Care Medicine. 2018;**197**(7):876-884. DOI: 10.1164/rccm.201709-1948OC

[12] Hoover DA, Capaldi DP, Sheikh K, Palma DA, Rodrigues GB, Dar AR, et al. Functional lung avoidance for individualized radiotherapy (FLAIR): Study protocol for a randomized, double-blind clinical trial. BMC Cancer. 2014;**14**(1):934. DOI: 10.1186/1471-2407-14-934

[13] Ontario Lung Association. Your Lungs, Your Life: Insights and Solutions to Lung Health in Ontario. 2012:1-24

[14] Canadian Cancer Society. Special topic: Pancreatic cancer. Canadian Cancer Statistics 2017. 2017:1-142

[15] Kovtunov KV, Truong ML, Barskiy DA, Koptyug IV, Coffey AM, Waddell KW, et al. Long-lived spin states for low-field hyperpolarized gas MRI. Chemistry. 2014;**20**(45):14629-14632. DOI: 10.1002/chem.201405063

[16] Kovtunov KV, Romanov AS, Salnikov OG, Barskiy DA, Chekmenev EY, Koptyug IV. Gas phase UTE MRI of propane and propene. Tomography. 2016;**2**(1):49-55. DOI: 10.18383/j. tom.2016.00112

[17] Ouriadov AV, Fox MS, Couch MJ, Li T, Ball IK, Albert MS. In vivo regional ventilation mapping using fluorinated gas MRI with an x-centric FGRE method. Magnetic Resonance in Medicine. 2015;**74**(2):550-557. DOI: 10.1002/mrm.25406

[18] Couch MJ, Ball IK, Li T, Fox MS, Littlefield SL, Biman B, et al. Pulmonary ultrashort echo time 19F MR imaging with inhaled fluorinated gas mixtures in healthy volunteers: Feasibility. Radiology. 2013;**269**(3):903-909. DOI: 10.1148/radiol.13130609

[19] Halaweish AF, Moon RE, Foster WM, Soher BJ, McAdams HP, MacFall JR, et al. Perfluoropropane gas as a magnetic resonance lung imaging contrast agent in humans. Chest. 2013;**144**(4):1300-1310. DOI: 10.1378/chest.12-2597

[20] Wang W, Nguyen NM, Yablonskiy DA, Sukstanskii AL, Osmanagic E, Atkinson JJ, et al. Imaging lung microstructure in mice with hyperpolarized 3He diffusion MRI. Magnetic Resonance in Medicine. 2011;**65**(3):620-626. DOI: 10.1002/mrm.22737

[21] Walvick RP, Roche JP, Reno AL, Gounis MJ, Albert MS. Evaluation of oxygen sensitivity of hyperpolarized helium imaging for the detection of pulmonary ischemia. Magnetic Resonance in Medicine. 2016;**75**(5):2050-2054. DOI: 10.1002/mrm.25714

[22] Driehuys B, Walker J, Pollaro J, Cofer GP, Mistry N, Schwartz D, et al. 3He MRI in mouse models of asthma. Magnetic Resonance in Medicine. 2007;**58**(5):893-900. DOI: 10.1002/mrm.21306

[23] Couch MJ, Ouriadov A, Santyr GE. Regional ventilation mapping of the rat lung using hyperpolarized 129Xe magnetic resonance imaging. Magnetic Resonance in Medicine. 2012;**68**(5):1623-1631. DOI: 10.1002/mrm.24152

[24] Wild JM, Woodhouse N, Paley MN, Fichele S, Said Z, Kasuboski L, et al. Comparison between 2D and 3D gradient-echo sequences for MRI of human lung ventilation with hyperpolarized 3He. Magnetic Resonance in Medicine. 2004;**52**(3):673-678. DOI: 10.1002/mrm.20164

[25] Dugas JP, Garbow JR, Kobayashi DK, Conradi MS. Hyperpolarized (3)He MRI of mouse lung. Magnetic Resonance in Medicine. 2004;**52**(6):1310-1317. DOI: 10.1002/mrm.20300

[26] Mugler JP, Brookeman JR. Method and System for Rapid Magnetic Resonance Imaging of Gases with Reduced Diffusion-Induced Signal Loss. Google Patents; 2006

[27] Ouriadov AV, Santyr GE. High spatial resolution hyperpolarized (3) He MRI of the rodent lung using a single breath X-centric gradient-recalled echo approach. Magnetic Resonance in Medicine. 2017;**78**(6):2334-2341. DOI: 10.1002/mrm.26602

[28] Altes TA, Meyer CH, Mata JF, Froh DK, Paget-Brown A, Gerald Teague W, et al. Hyperpolarized helium-3 magnetic resonance lung imaging of non-sedated

infants and young children: A proof-of-concept study. Clinical Imaging. 2017;**45**:105-110. DOI: 10.1016/j.clinimag.2017.04.004

[29] Bergin CJ, Pauly JM, Macovski A. Lung parenchyma: Projection reconstruction MR imaging. Radiology. 1991;**179**(3):777-781. DOI: 10.1148/radiology.179.3.2027991

[30] Chen BT, Brau AC, Johnson GA. Measurement of regional lung function in rats using hyperpolarized 3helium dynamic MRI. Magnetic Resonance in Medicine. 2003;**49**(1):78-88. DOI: 10.1002/mrm.10336

[31] Viallon M, Berthezene Y, Callot V, Bourgeois M, Humblot H, Briguet A, et al. Dynamic imaging of hyperpolarized3He distribution in rat lungs using interleaved-spiral scans. NMR in Biomedicine. 2000;**13**(4):207-213. DOI: 10.1002/1099-1492 (200006)13:4<207::aid-nbm641>3.0.co;2-g

[32] Salerno M, Altes TA, Brookeman JR, de Lange EE, Mugler JP 3rd. Dynamic spiral MRI of pulmonary gas flow using hyperpolarized (3)He: Preliminary studies in healthy and diseased lungs. Magnetic Resonance in Medicine. 2001;**46**(4):667-677

[33] Gurney PT, Hargreaves BA, Nishimura DG. Design and analysis of a practical 3D cones trajectory. Magnetic Resonance in Medicine. 2006;**55**(3):575-582. DOI: 10.1002/mrm.20796

[34] Wang JX, Ouriadov A, Stainsby J, Parraga G, Santyr G. 3D hyperpolarized 3He imaging of human lung with isotropic spatial resolution using 3D-cones. In: Proceedings of the 17th Annual Meeting of ISMRM; Stockholm, Sweden. 2009. p. 4601

[35] Zhang Z, Ouriadov AV, Willson C, Balcom BJ. Membrane gas diffusion measurements with MRI. Journal of Magnetic Resonance. 2005;**176**(2):215-222. DOI: 10.1016/j.jmr.2005.06.009

[36] Shattuck MD, Gewalt SL, Glover GH, Hedlund LW, Johnson GA. MR microimaging of the lung using volume projection encoding. Magnetic Resonance in Medicine. 1997;**38**(6):938-942

[37] Fox MS, Ouriadov A, Santyr GE. Comparison of hyperpolarized 3He and 129Xe MRI for the measurement of absolute ventilated lung volume in rats. Magnetic Resonance in Medicine. 2014;**71**(3):1130-1136. DOI: 10.1002/mrm.24746

[38] Ouriadov AV, Kennan R, Slipetz D, Santyr G, Williams D, Rutt BK, et al. In-vivo hyperpolarized 3He lung imaging in mice using x-centric fGRE sequence and custom-designed flexivent ventilator. In: Proceedings of the 16th Annual Meeting of ISMRM; Toronto, Canada. 2008. p. 3789

[39] Santyr GE, Lam WW, Parra-Robles JM, Taves TM, Ouriadov AV. Hyperpolarized noble gas magnetic resonance imaging of the animal lung: Approaches and applications. Journal of Applied Physics. 2009;**105**(10):102004. DOI: 10.1063/1.3112143

[40] Moller HE, Chen XJ, Saam B, Hagspiel KD, Johnson GA, Altes TA, et al. MRI of the lungs using hyperpolarized noble gases. Magnetic Resonance in Medicine. 2002;**47**(6):1029-1051. DOI: 10.1002/mrm.10173

[41] Mugler JP 3rd, Altes TA. Hyperpolarized 129Xe MRI of the human lung. Journal of Magnetic Resonance Imaging. 2013;**37**(2):313-331. DOI: 10.1002/jmri.23844

[42] Brown RW, Cheng YCN, Haacke EM, Thompson MR, Venkatesan R. Magnetic Resonance Imaging: Physical

Principles and Sequence Design. 2nd ed. Hoboken, New Jersey: Wiley Blackwell; 2014. DOI: 10.1002/978111 8633953

[43] Foster-Gareau P, Heyn C, Alejski A, Rutt BK. Imaging single mammalian cells with a 1.5 T clinical MRI scanner. Magnetic Resonance in Medicine. 2003;**49**(5):968-971. DOI: 10.1002/mrm.10417

[44] Chen XJ, Möller HE, Chawla MS, Cofer GP, Driehuys B, Hedlund LW, et al. Spatially resolved measurements of hyperpolarized gas properties in the lung in vivo. Part II: T*2. Magnetic Resonance in Medicine. 1999;**42**(4):729-737. DOI: 10.1002/(SICI)1522-2594(199910)42:4<729::AID-MRM15>3.0.CO;2-2

[45] Saam B, Happer W, Middleton H. Nuclear relaxation of ^{3}He in the presence of O_2. Physical Review A. 1995;**52**(1):862-865

[46] Deninger AJ, Eberle B, Ebert M, Grossmann T, Heil W, Kauczor HU, et al. Quantification of regional intrapulmonary oxygen partial pressure evolution during apnea by He-3 MRI. Journal of Magnetic Resonance. 1999;**141**(2):207-216. DOI: 10.1006/jmre.1999.1902

[47] Ouriadov AV, Lam WW, Santyr GE. Rapid 3-D mapping of hyperpolarized 3He spin-lattice relaxation times using variable flip angle gradient echo imaging with application to alveolar oxygen partial pressure measurement in rat lungs. Magma. 2009;**22**(5):309-318. DOI: 10.1007/s10334-009-0181-3

[48] Santyr GE, Lam WW, Ouriadov A. Rapid and efficient mapping of regional ventilation in the rat lung using hyperpolarized 3He with flip angle variation for offset of RF and relaxation (FAVOR). Magnetic Resonance in Medicine. 2008;**59**(6):1304-1310. DOI: 10.1002/mrm.21582

[49] Nishimura DG. Principles of Magnetic Resonance Imaging. Stanford University; 1996

[50] Chen XJ, Moller HE, Chawla MS, Cofer GP, Driehuys B, Hedlund LW, et al. Spatially resolved measurements of hyperpolarized gas properties in the lung in vivo. Part I: Diffusion coefficient. Magnetic Resonance in Medicine. 1999;**42**(4):721-728. DOI: 10.1002/(SICI)1522-2594(199910)42:4<721::AID-MRM14>3.0.CO;2-D

[51] Miller G, Altes T, Brookeman J, De Lange E, Mugler Iii J. Hyperpolarized 3He lung ventilation imaging with B 1-inhomogeneity correction in a single breath-hold scan. Magnetic Resonance Materials in Physics, Biology and Medicine. 2004;**16**(5):218-226

[52] Zhao L, Mulkern R, Tseng CH, Williamson D, Patz S, Kraft R, et al. Gradient-echo imaging considerations for hyperpolarized 129Xe MR. Journal of Magnetic Resonance—Series B. 1996;**113**(2):179-183

[53] Stejskal EO, Tanner JE. Spin diffusion measurements: Spin echoes in the presence of a time-dependent field gradient. The Journal of Chemical Physics. 1965;**42**(1):288-292

[54] Danneman PJ, Suckow MA, Brayton C. The Laboratory Mouse. CRC Press; 2012

[55] Chen BT, Yordanov AT, Johnson GA. Ventilation-synchronous magnetic resonance microscopy of pulmonary structure and ventilation in mice. Magnetic Resonance in Medicine. 2005;**53**(1):69-75. DOI: 10.1002/mrm.20307

[56] Lundblad L, Thompson-Figueroa J, Leclair T, G Irvin C, Bates J. Thoracic gas volume measurements in paralyzed mice. Annals of Biomedical Engineering. 2004;**32**(10):1420-1427. DOI: 10.1114/B:ABME.0000042229.41098.6a

[57] Han H, MacGregor RP, Balcom BJ. Pure phase encode magnetic field gradient monitor. Journal of Magnetic Resonance. 2009;**201**(2):212-217. DOI: 10.1016/j.jmr.2009.09.011

[58] Dominguez-Viqueira W, Ouriadov A, O'Halloran R, Fain SB, Santyr GE. Signal-to-noise ratio for hyperpolarized (3)He MR imaging of human lungs: A 1.5 T and 3 T comparison. Magnetic Resonance in Medicine. 2011;**66**(5): 1400-1404. DOI: 10.1002/mrm.22920

[59] Rose A. The sensitivity performance of the human eye on an absolute scale. Journal of the Optical Society of America. 1948;**38**(2):196-208

[60] Haacke EM, Brown RW, Thompson MR, Venkatesan R. Magnetic Resonance Imaging: Physical Principles and Sequence Design. Magnetic Resonance Imaging: Physical Principles and Sequence Design. New York: NY John Wiley & Sons Ltd; 1999. DOI: 10.1002/9781118633953.ch1

[61] Stenger VA, Noll DC, Boada FE. Partial Fourier reconstruction for three-dimensional gradient echo functional MRI: Comparison of phase correction methods. Magnetic Resonance in Medicine. 1998;**40**(3):481-490

[62] Haacke EM, Lindskogj ED, Lin W. A fast, iterative, partial-fourier technique capable of local phase recovery. Journal of Magnetic Resonance (1969). 1991; **92**(1):126-145. DOI: 10.1016/0022-2364 (91)90253-p

[63] Altes TA, Meyer CH, Mata JH, Froh D, Paget-Brown A, Fain S, et al. Hyperpolarized Helium-3 MR imaging of a non-sedated infant: A proof-of-concept study: Preliminary experience. In: Proceedings of the 20th Annual Meeting of ISMRM. Melbourne, Australia; 2012. p. P1355

[64] Chang YV, Quirk JD, Yablonskiy DA. In vivo lung morphometry with accelerated hyperpolarized (3) He diffusion MRI: A preliminary study. Magnetic Resonance in Medicine. 2015; **73**(4):1609-1614. DOI: 10.1002/mrm.25284

[65] Chan HF, Stewart NJ, Parra-Robles J, Collier GJ, Wild JM. Whole lung morphometry with 3D multiple b-value hyperpolarized gas MRI and compressed sensing. Magnetic Resonance in Medicine. 2017;**77**(5):1916-1925. DOI: 10.1002/mrm.26279

[66] Zhang H, Xie J, Xiao S, Zhao X, Zhang M, Shi L, et al. Lung morphometry using hyperpolarized (129) Xe multi-b diffusion MRI with compressed sensing in healthy subjects and patients with COPD. Medical Physics. 2018;**45**(7):3097-3108. DOI: 10.1002/mp.12944

[67] Westcott A, McCormack DG, Parraga G, Ouriadov A. Advanced pulmonary MRI to quantify alveolar and acinar duct abnormalities: Current status and future clinical applications. Journal of Magnetic Resonance Imaging. 2019;(0):0. DOI: 10.1002/nbm.3165

[68] Norquay G, Collier GJ, Rao M, Stewart NJ, Wild JM. 129Xe-Rb spin-exchange optical pumping with high photon efficiency. Physical Review Letters. 2018;**121**(15): 153201. DOI: 10.1103/PhysRevLett.121.153201

[69] Goodson BM, Ranta K, Skinner JG, Coffey AM, Nikolaou P, Gemeinhardt M, et al. Chapter 2—The physics of hyperpolarized gas MRI A2. In: Albert MS, Hane FT, editors. Hyperpolarized and Inert Gas MRI. Boston: Academic Press; 2017. pp. 23-46. DOI: 10.1016/B978-0-12-803675-4.00002-6

[70] Wild JM, Collier G, Marshall H, Smith L, Norquay G, Swift AJ, et al. P283 hyperpolarised gas MRI—A pathway to Clinical diagnostic imaging. Thorax. 2015;**70**(Supp. 3):

A220.3-A220A1. DOI: 10.1136/ thoraxjnl-2015-207770.419

[71] 129Xe MRI Clinical Trials Consortium. [Internet]. 2018. https://c ircchmcorg/XeMRICTC.

[72] Rao MR, Stewart NJ, Griffiths PD, Norquay G, Wild JM. Imaging human brain perfusion with inhaled hyperpolarized 129Xe MR imaging. Radiology. 2018;**286**(2):659-665. DOI: 10.1148/radiol.2017162881

[73] Westcott A, Guo F, Parraga G, Ouriadov A. Rapid single-breath hyperpolarized Noble gas MRI based biomarkers of airspace enlargement. Journal of Magnetic Resonance Imaging. 2018;**2018**. DOI: 10.1002/ jmri.26574

[74] Svenningsen S, Kirby M, Starr D, Leary D, Wheatley A, Maksym GN, et al. Hyperpolarized (3) He and (129) Xe MRI: Differences in asthma before bronchodilation. Journal of Magnetic Resonance Imaging. 2013; **38**(6):1521-1530. DOI: 10.1002/ jmri.24111

[75] Xu X, Norquay G, Parnell SR, Deppe MH, Ajraoui S, Hashoian R, et al. Hyperpolarized 129Xe gas lung MRI-SNR and T2* comparisons at 1.5 T and 3 T. Magnetic Resonance in Medicine. 2012;**68**(6):1900-1904. DOI: 10.1002/ mrm.24190

[76] Mugler JP, Driehuys B, Brookeman JR, Cates GD, Berr SS, Bryant RG, et al. MR imaging and spectroscopy using hyperpolarized 129Xe gas: Preliminary human results. Magnetic Resonance in Medicine. 1997;**37**(6):809-815. DOI: 10.1002/mrm.1910370602

[77] Sakai K, Bilek AM, Oteiza E, Walsworth RL, Balamore D, Jolesz FA, et al. Temporal dynamics of hyperpolarized 129Xe resonances in living rats. Journal of Magnetic Resonance. Series B. 1996;**111**(3): 300-304

[78] Ruppert K, Brookeman JR, Hagspiel KD, Driehuys B, Mugler JP. NMR of hyperpolarized129Xe in the canine chest: Spectral dynamics during a breath-hold. NMR in Biomedicine. 2000;**13**(4):220-228. DOI: 10.1002/ 1099-1492(200006)13:4<220::aid-nbm638>3.0.co;2-f

[79] Kaushik SS, Robertson SH, Freeman MS, He M, Kelly KT, Roos JE, et al. Single-breath clinical imaging of hyperpolarized (129)Xe in the airspaces, barrier, and red blood cells using an interleaved 3D radial 1-point Dixon acquisition. Magnetic Resonance in Medicine. 2016;**75**(4):1434-1443. DOI: 10.1002/mrm.25675

[80] Driehuys B, Cofer GP, Pollaro J, Mackel JB, Hedlund LW, Johnson GA. Imaging alveolar–capillary gas transfer using hyperpolarized 129Xe MRI. Proceedings of the National Academy of Sciences. 2006;**103**(48):18278-18283. DOI: 10.1073/pnas.0608458103

[81] Fox MS, Ouriadov A, Thind K, Hegarty E, Wong E, Hope A, et al. Detection of radiation induced lung injury in rats using dynamic hyperpolarized (129)Xe magnetic resonance spectroscopy. Medical Physics. 2014;**41**(7):072302. DOI: 10.1118/1.4881523

[82] Doganay O, Matin T, Chen M, Kim M, McIntyre A, McGowan DR, et al. Time-series hyperpolarized xenon-129 MRI of lobar lung ventilation of COPD in comparison to V/Q-SPECT/CT and CT. European Radiology. 2018. DOI: 10.1007/s00330-018-5888-y

[83] Mazzanti ML, Walvick RP, Zhou X, Sun Y, Shah N, Mansour J, et al. Distribution of hyperpolarized xenon in the brain following sensory stimulation: Preliminary MRI findings. PLoS One. 2011;**6**(7):e21607. DOI: 10.1371/journal. pone.0021607

[84] Zeng Q, Guo Q, Yuan Y, Yang Y, Zhang B, Ren L, et al. Mitochondria

targeted and intracellular biothiol triggered hyperpolarized (129)Xe magnetofluorescent biosensor. Analytical Chemistry. 2017;**89**(4): 2288-2295. DOI: 10.1021/acs. analchem.6b03742

[85] Zanette B, Stirrat E, Jelveh S, Hope A, Santyr G. Physiological gas exchange mapping of hyperpolarized (129) Xe using spiral-IDEAL and MOXE in a model of regional radiation-induced lung injury. Medical Physics. 2018; **45**(2):803-816. DOI: 10.1002/mp.12730

[86] Doganay O, Wade T, Hegarty E, McKenzie C, Schulte RF, Santyr GE. Hyperpolarized (129) Xe imaging of the rat lung using spiral IDEAL. Magnetic Resonance in Medicine. 2016;**76**(2): 566-576. DOI: 10.1002/mrm.25911

[87] Chang YV, Conradi MS. Relaxation and diffusion of perfluorocarbon gas mixtures with oxygen for lung MRI. Journal of Magnetic Resonance. 2006; **181**(2):191-198. DOI: 10.1016/j. jmr.2006.04.003

[88] Couch MJ, Fox MS, Viel C, Gajawada G, Li T, Ouriadov AV, et al. Fractional ventilation mapping using inert fluorinated gas MRI in rat models of inflammation and fibrosis. NMR in Biomedicine. 2016;**29**(5):545-552. DOI: 10.1002/nbm.3493

[89] Gutberlet M, Kaireit TF, Voskrebenzev A, Lasch F, Freise J, Welte T, et al. Free-breathing dynamic (19)F gas MR imaging for mapping of regional lung ventilation in patients with COPD. Radiology. 2018;**286**(3): 1040-1051. DOI: 10.1148/ radiol.2017170591

[90] Couch MJ, Ouriadov AV, Albert MS. Chapter 18—Pulmonary imaging using 19f mri of inert fluorinated gases. In: Hyperpolarized and Inert Gas MRI. Boston: Academic Press; 2017. pp. 279-292. DOI: 10.1016/B978-0- 12-803675-4.00018-X

[91] Deninger AJ, Månsson S, Petersson JS, Pettersson G, Magnusson P, Svensson J, et al. Quantitative measurement of regional lung ventilation using 3He MRI. Magnetic Resonance in Medicine. 2002;**48**(2): 223-232. DOI: 10.1002/mrm.10206

[92] Berberan-Santos MN, Bodunov EN, Valeur B. Mathematical functions for the analysis of luminescence decays with underlying distributions 1. Kohlrausch decay function (stretched exponential). Chemical Physics. 2005; **315**(1–2):171-182. DOI: 10.1016/j. chemphys.2005.04.006

[93] Abascal JFPJ, Desco M, Parra-Robles J. Incorporation of Prior Knowledge of the Signal Behavior into the Reconstruction to Accelerate the Acquisition of MR Diffusion Data. ArXiv e-prints [Internet]. 2017; 1702. Available from: http://adsabs.harvard.ed u/abs/2017arXiv170202743A

[94] Charles C, Jones2 RW, Halaweish AF, Ainslie MD. Parallel imaging for short breath hold times in perfluorinated gas imaging of the lung [abstract]. In: Proceedings of the 23rd Annual Meeting of ISMRM; Toronto, Canada. 2015. p. 3984